ELMORE

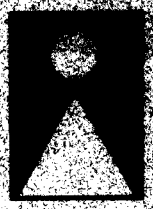

NATIONAL
OPTICAL
ASTRONOMY
OBSERVATORY

Preprint Series

NOAO Preprint No. 889

INSTRUMENTATION FOR ASTROPHYSICAL SPECTROPOLARIMETRY

Christoph U. Keller
(National Solar Observatory, National Optical Astronomy Observatory)

Presented at: The IAC Winterschool on
Astrophysical Spectropolarimetry
Cambridge University
(November 2000)

February 2001

Instrumentation for Astrophysical Spectropolarimetry

By CHRISTOPH U. KELLER

National Solar Observatory, 950 N. Cherry Ave., Tucson, AZ 85719, USA

Astronomical spectropolarimetry is performed from the X-ray to the radio regimes of the electromagnetic spectrum. The following chapter deals with instruments and their components that are used in the wavelength range from 300 nm to 20 μm. After introducing the terminology and formalisms that are used in the context of astronomical spectropolarimeters, I discuss the most widely used optical components. These include crystal and sheet polarizers, fixed monochromatic and achromatic retarders, and variable retarders such as liquid crystals and photoelastic modulators. Since polarimetric measurements are often limited by systematic errors rather than statistical errors due to photon noise, I deal with these instrumentally induced errors in detail. Among these errors, I discuss instrumental polarization of various kinds and chromatic and angle of incidence errors of optical components. I close with a few examples of successful, modern night-time and solar spectropolarimeters.

1. Introduction

1.1. *Scope of chapter*

Astronomical polarimetry is performed over a large fraction of the electromagnetic spectrum, from X-rays to radio waves. The following chapter is restricted to the optical range that can be observed from the ground, i.e. 300 nm to 20 μm. Far-infrared polarimetry is described by Hildebrand in this volume. Information on polarimetry in the X-ray and radio regimes can be found in Tinbergen (1996).

Furthermore, the following text focuses on instruments for spectropolarimetry, i.e. the instrumental aspects of polarimetry with a spectral resolution that resolves spectral lines, either with a spectrograph or a filter, i.e. a spectral resolution of $\lambda/\delta\lambda = R > 10,000$. However, it needs to be remembered that polarimetry using the same optical techniques is often performed at low spectral resolution. Finally, the text mostly deals with high-precision polarimetry, i.e. sensitivities of the order 10^{-3} or better, and most examples are from solar observations.

This introduction to instrumentation for astrophysical spectropolarimetry is based on a series of 5 lectures. The viewgraphs shown in those lectures can be found at `www.noao.edu/noao/staff/keller`.

1.2. *Brief history of optics and instruments for spectropolarimetry*

Over the centuries, many people have contributed to the development of instruments to measure the polarization of astronomical objects. Table 1 lists some of them with an emphasis on their contribution to instrumentation. In addition, it also lists some of the failed attempts to detect polarization in order to show how early scientists tried to use spectropolarimetry in astrophysics.

Historically important contributions to polarized light have been collected by Swindell (1975) and Billings (1990). Livingston (1993) included some historically relevant papers on astronomical polarimeters.

1669	Erasmus Bartholinus discovers double refraction in calcite
1690	Christian Huygens discovers extinction with two crossed calcites
1808	Etienne-Louis Malus discovers polarization from reflection
1812	David Brewster discovers angle of reflection where light is totally polarized and finds relation with index of refraction
1818	Augustin Jean Fresnel and Dominique Francois Arago find the transverse nature of polarization
1828	William Nicol invents the first calcite polarizing prism
1852	George Gabriel Stokes introduces the Stokes parameters
1852	William Bird Herapath and his student Phelps find polarizing crystals in the urine of a dog that was fed quinine when iodine was dripped into it
1858	E. Liais discovers linear polarization in the solar corona during an eclipse
1875	John Kerr discovers the birefringence of isotropic materials when an external electrical field is applied
1906	George E. Hale visually searches for linear polarization in sunspots without success
1908	George E. Hale finds circular and linear polarization in sunspots using photographic plates
1910	W.H. Wright finds no polarization due to the Zeeman effect in stellar hydrogen line spectra
1913	P.W. Merrill finds no polarization due to the Zeeman effect in stellar hydrogen line spectra
1928	Edwin H. Land develops the first sheet polarizer using herapathite crystals
1933	Hale and collaborators fail to obtain photo-electric measurements of the circular polarization due to the Zeeman effect in the sun
1941	R. Clark Jones introduces 2 by 2 complex matrices to describe the effect of a crystalline plate on the state of polarization
1943	Hans Mueller introduces four by four real matrices to describe the influence of depolarizing optics
1944	Bernard Lyot develops the birefringent filter
1946	S.M. MacNeille invents the thin-film polarizing cube beam splitter
1946	S. Chandrasekhar introduces Stokes parameters to astrophysics and includes polarization in radiative transfer
1947	Horace W. Babcock discovers circular polarization in 78 Vir
1953	K.O. Kiepenheuer and Babcock and Babcock use photo-electric spectropolarimeters to measure magnetic fields all over the sun
1958	Audouin Dollfus develops a modulating polarizer that reaches a sensitivity of 10^{-5} using a rotating waveplate
1966	M. Billardon and J. Badoz invent the photoelastic modulator
1969	James C. Kemp predicts that photoelastic modulators could measure the circular polarization of astronomical objects with an accuracy of 10^{-6}

TABLE 1. Timetable of important events in the development of astronomical spectropolarimeters.

1.3. *Books on polarimetry*

Various books have been written on polarimetry in general. The classical book by Shurcliff (1962) is compact and contains many historical references, but it is not in print anymore. Collett (1993) is extensive and easy to read, but the book is rather expensive. Clarke and Grainger (1971), Azzam and Bashara (1987), and Kliger et al. (1990) are some of the other books that deal with polarimetry. Only a few books deal specifically with astronomical polarimetry. The conference proceedings by Gehrels (1974) contain interesting papers on instrumentation, although many are nowadays of mostly historical interest. Two recent monographs dealing specifically with astronomical polarimetry are those by Tinbergen (1996) and Leroy (2000). Leroy's book is an introduction to po-

larization in astrophysics that avoids equations to remain readable for a wide audience. Tinbergen's text is aimed at a higher level but leaves many interesting equations to be derived as exercises.

2. Principles of optical polarization measurements

2.1. *Terminology*

While the Jones and Mueller formalisms are explained in detail by Landi Degl'Innocenti in this volume, the following paragraphs will briefly introduce the terminology and definitions used here and highlight issues associated with instrumentation. A formalism that is not reviewed here is the Poincaré sphere. While that approach has its advantages, it has become considerably less important with fast computers that can easily deal with large sets of Mueller matrices. An extended review of the Poincaré sphere formalism has been given by Ramachandran and Ramaseshan (1962).

2.1.1. *Stokes parameters, vectors, and Mueller matrices*

Mueller matrices describe the (linear) transformation between Stokes vectors (formed by grouping the four Stokes parameters into a single vector) associated with optical elements and surfaces, i.e.

$$\boldsymbol{I}' = \mathsf{M}\boldsymbol{I}\,, \tag{2.1}$$

where the Stokes vector consists of the following Stokes parameters

$$\boldsymbol{I} = \begin{pmatrix} I \\ Q \\ U \\ V \end{pmatrix} = \begin{pmatrix} I_1 \\ I_2 \\ I_3 \\ I_4 \end{pmatrix}\,. \tag{2.2}$$

The latter form of the Stokes vector components is useful when applying methods of linear algebra to Stokes vectors. Extensive examples of Stokes vectors are given by Shurcliff (1962).

Mueller matrices have the following form:

$$\mathsf{M} = \begin{pmatrix} M_{11} & M_{12} & M_{13} & M_{14} \\ M_{21} & M_{22} & M_{23} & M_{24} \\ M_{31} & M_{32} & M_{33} & M_{34} \\ M_{41} & M_{42} & M_{43} & M_{44} \end{pmatrix}\,. \tag{2.3}$$

A *normalized* Mueller matrix is obtained by scaling the matrix such that the upper left element is equal to one. Some useful examples of Mueller matrices are given in the following sections. Extensive lists of Mueller matrices are given by Shurcliff (1962) and Kliger et al. (1990).

When a beam of light passes through N optical elements, each described by a Mueller matrix M_i, the combined Mueller matrix M' of the whole assembly is given by

$$\mathsf{M}' = \mathsf{M}_N\mathsf{M}_{N-1}\cdots\mathsf{M}_2\mathsf{M}_1\,. \tag{2.4}$$

Note the reversed order of the Mueller matrices as compared to the order in which the light passes through the optical elements. This order is important since Mueller matrices do not commute in general.

Rotation of elements described by Mueller matrices are given by

$$\mathsf{M}' = \mathsf{R}(-\alpha)\mathsf{M}\mathsf{R}(\alpha)\,, \tag{2.5}$$

where α is the rotation angle, and the rotation matrix R is given by

$$\mathsf{R}(\alpha) = \begin{pmatrix} 1 & 0 & 0 & 0 \\ 0 & \cos 2\alpha & \sin 2\alpha & 0 \\ 0 & -\sin 2\alpha & \cos 2\alpha & 0 \\ 0 & 0 & 0 & 1 \end{pmatrix} . \tag{2.6}$$

The formalism for rotating Mueller matrices given above cannot be applied blindly. In particular, one has to remember that this formalism assumes that we keep the same coordinate system for the incoming and outgoing beams. However, when reflections are considered, the convention is to change the coordinate system for the reflected beam as compared to the incoming beam (see Landi Degl'Innocenti in this volume). The Mueller matrix for an ideal reflection at normal incidence is given by

$$\mathsf{M} = \begin{pmatrix} 1 & 0 & 0 & 0 \\ 0 & 1 & 0 & 0 \\ 0 & 0 & -1 & 0 \\ 0 & 0 & 0 & -1 \end{pmatrix} , \tag{2.7}$$

which indicates nothing but the change in the coordinate system for the Stokes vector. Therefore, the above formalism for calculating the Mueller matrix of rotated optical components cannot be directly applied when reflections are involved. In that case, it is often easier to consider the rotation of Stokes vectors (to which the rotation matrix R can be applied).

Let us consider an example. It is well known that successive reflections off two mirrors will not modify the polarization if the angles of incidence are the same for both reflections and if the surface normal of the second mirror is perpendicular to the plane of incidence of the first mirror. This principle is sometimes used to compensate the instrumental polarization introduced by a single reflection. If M_r is the Mueller matrix describing the reflection off a single mirror, a naive use of the above formalism would lead us to write the combined Mueller matrix of both mirrors as

$$\mathsf{M}' = \mathsf{R}(-90°)\mathsf{M}_r\mathsf{R}(+90°)\mathsf{M}_r . \tag{2.8}$$

Using the diagonal matrix given above for normal incidence as the mirror reflection Mueller matrix M_r shows immediately that the above equation is incorrect and should be replaced by

$$\mathsf{M}' = \mathsf{R}(+90°)\mathsf{M}_r\mathsf{R}(+90°)\mathsf{M}_r . \tag{2.9}$$

The reason for this is that the Mueller matrix for reflection implies a change in coordinate system that requires a change in the sign of the angle for the rotation matrix.

Finally, Stokes vectors and Mueller matrices operate on intensities and their differences, i.e. incoherent superpositions of light, they are not adequate to describe interference nor diffraction effects. However, they are ideally suited to describe partially polarized and unpolarized light.

2.1.2. *Jones vectors and matrices*

The Jones calculus is the adequate way to describe the coherent superposition of polarized light because it operates on amplitudes rather than on intensities. However, Jones vectors and matrices can only describe 100% polarized light because a monochromatic wave is always 100% polarized.

The electrical field vector of a monochromatic electromagnetic wave traveling along the z axis of a right-handed coordinate system can be decomposed into its x and y

components

$$\mathrm{Re}E_x\,,\mathrm{Re}E_y\,, \tag{2.10}$$

where E_x and E_y are complex quantities with an amplitude and a phase.

The Jones vectors contain the complex amplitude electrical field components in the form

$$\boldsymbol{E} = \begin{pmatrix} E_x \\ E_y \end{pmatrix}\,. \tag{2.11}$$

Note that amplitudes are not observed directly by detectors in the wavelength range considered here. Therefore, observables always depend on products of Jones vector components such as $|\boldsymbol{E}|^2$.

The transfer of 100% polarized light through an optical medium is described by 2 by 2 complex matrices. Combined Jones matrices describing a series of optical elements are equal to the matrix product of the individual Jones matrices in the same way as with Mueller matrices. Examples of various Jones matrices are given in the following sections. Extensive lists have been prepared by Shurcliff (1962) and Kliger et al. (1990).

The rotation of Jones matrices is given by

$$\mathsf{J}' = \mathsf{R}(-\alpha)\mathsf{J}\mathsf{R}(\alpha)\,, \tag{2.12}$$

where the rotation matrix R is given by

$$\mathsf{R} = \begin{pmatrix} \cos\theta & \sin\theta \\ -\sin\theta & \cos\theta \end{pmatrix}\,. \tag{2.13}$$

Any Jones matrix can be transformed into the corresponding Mueller matrix using the following relation (Azzam & Bashara 1987):

$$\mathsf{M} = \mathsf{B}\,(\mathsf{J}\otimes\mathsf{J}^*)\,\mathsf{B}^{-1}\,, \tag{2.14}$$

where * indicates the complex conjugate,

$$\mathsf{B} = \begin{pmatrix} 1 & 0 & 0 & 1 \\ 1 & 0 & 0 & -1 \\ 0 & 1 & 1 & 0 \\ 0 & i & -i & 0 \end{pmatrix}\,, \tag{2.15}$$

and $\otimes$ is the tensor product. For matrices B and C with N by N elements, the tensor product is a N^2 by N^2 matrix given by

$$\mathsf{A} = \mathsf{B}\otimes\mathsf{C}\,, \tag{2.16}$$

where

$$a_{i+(j-1)N,k+(l-1)N} = b_{i,k}c_{j,l}\,. \tag{2.17}$$

While the Jones matrix has 8 independent parameters, the absolute phase information is lost in the Mueller matrix, leading to only seven independent matrix elements for a Mueller matrix derived from a Jones matrix. A general Mueller matrix has 8 degrees of freedom, the additional degree being related to the transfer of unpolarized light.

2.1.3. *TE and TM waves, s and p polarization*

In the context of optics manufacturing and testing, a terminology different from Stokes vectors and Mueller matrices is used (see Fig. 1). We consider the plane of incidence formed by the normal to the surface and the direction of the incoming light. If the electrical field of the incoming wave is in the plane of incidence, then the magnetic field must be transverse to it, and this is therefore called a TM (transverse magnetic) or *p*-

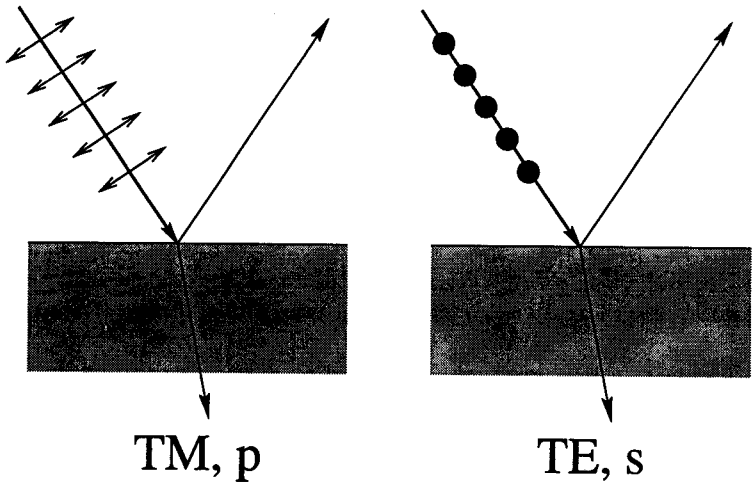

FIGURE 1. Definition of transverse magnetic (TM), transverse electric (TE), p, and s polarized waves. The definitions are only valid in the context of a light beam being reflected off or transmitted through an interface between two materials with different indices of refraction at non-normal incidence.

polarized wave (p for parallel). The other one is the TE (transverse electric) or *s-polarized* (s for 'senkrecht'= perpendicular in German) wave.

To fully characterize the influence of an interface between two materials (e.g. air to metal), not only the reflectivities for s and p polarization need to be considered, but also the phase delay between s and p polarized light introduced by the interface. In general, there will also be absorption for the transmitted light, i.e. the energies of the reflected and the transmitted beam are not equal to the energy of the incoming beam. Purely dielectric media do not absorb energy.

2.1.4. *Polarization sensitivity and accuracy*

In the following, we will distinguish between polarization *sensitivity* and *accuracy*. Polarization sensitivity describes the magnitude of a small polarization signal on top of a big background that can just be detected. An adequate measure of the polarization sensitivity is the standard deviation of a polarized spectrum that is known to have no spectral variation of the polarization signal. Polarization accuracy is the magnitude of the absolute error in the polarization measurement. Both are typically expressed as a fraction of the intensity. These definitions are in analogy to definitions used in photometry.

2.2. *Polarized ray-tracing*

To simulate the design of a polarimeter, we need to calculate the influence of the telescope, instrument, and polarimeter on the polarization of the incoming light. While initial simulations can assume a single ray passing through the optical components along the optical axis, more accurate simulations require that many rays are traced through the optics, similar to what is done for general optical design. The polarization aspect of ray-tracing can often be described by a series of Mueller matrices that can be combined into a single Mueller matrix for each ray corresponding to one point in the field of view and one point in the pupil. The Mueller matrices corresponding to all the points in the pupil can then be averaged into a single Mueller matrix (incoherent superposition) that is equivalent to the average over the point-spread function (PSF) in the final focus for a single point in the field of view.

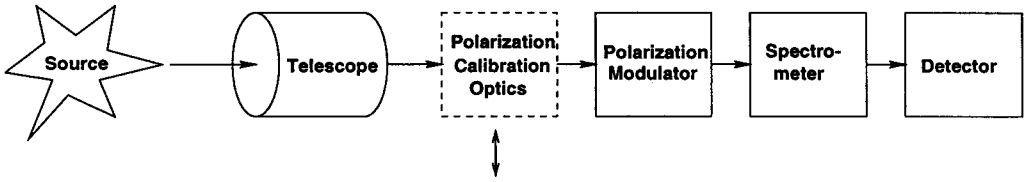

FIGURE 2. General layout of an astronomical spectropolarimeter: Light from a source passes through the telescope. A polarization calibration package can be inserted into the beam to calibrate the polarimeter and the rest of the instrument. During observations of the source, the calibration optics is not in the beam. The polarization modulator translates the polarization information into spatial and/or temporal variations. The beam(s) then pass through the spectrometer and are recorded by the detector.

A more accurate calculation requires that the various beams are combined coherently in the focal plane, something the Mueller calculus cannot describe. If one uses the Jones formalism in the equivalent way as the Mueller formalism above, one obtains the Jones matrix that corresponds to the center of the PSF. This method can be expanded to calculate the Mueller matrix at any position within the PSF for a given point in the field of view by calculating the Fourier transform of the Jones matrices in the exit pupil (Sánchez Almeida & Martínez Pillet 1992).

However, the latter approach is only valid for slow beams where one can assume that all rays that are averaged are almost parallel in the final focus. For fast beams, a more extensive way of polarized raytracing has to be used. Chipman (1995) developed such a method by extending the Jones vector approach to three complex components of the electric field. An optical element is described by a 3 by 3 complex matrix, and the rays are described by a complex vector with three components. While this approach is very general and can calculate complex and fast optics, it is normally not needed for astronomical instruments.

2.3. *Basic polarimeters*

In general, polarimeters consist of optical elements such as retarders and polarizers that change the polarization state of the incoming light in a controlled way (see Fig. 2). The detectors only measure intensities, at least for the part of the spectrum considered here. The various intensity measurements are then combined to retrieve the polarization state of the incoming light. Polarimeters differ mostly by the way that the polarization modulator works. In addition, a good polarimeter should also include optics for the polarization calibration, i.e. optics with very well known polarization characteristics that can be temporarily inserted in front of the polarization modulator.

2.3.1. *Rotating waveplate polarimeter*

A simple polarimeter can be built using a rotating waveplate and a linear polarizer (see Fig 3). The Mueller matrix calculus introduced above and the Mueller matrices for a retarder and a linear polarizer (see below) allow us to determine the intensity seen by the detector as a function of retardance δ and position angle θ of the rotating retarder. The intensity seen by the detector is given by

$$I' = \frac{1}{2}\left(I + \frac{Q}{2}\left((1+\cos\delta) + (1-\cos\delta)\cos 4\theta\right) + \frac{U}{2}(1-\cos\delta)\sin 4\theta - V\sin\delta\sin 2\theta\right) . \tag{2.18}$$

From this equation, we can deduce the following:

- only the terms that depend on θ will lead to a modulated signal;

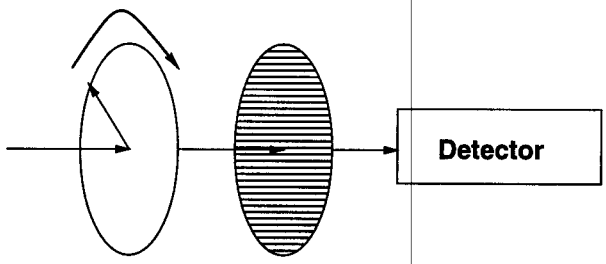

FIGURE 3. A simple polarimeter consisting of a rotating retarder and a fixed linear polarizer, which together make up the modulator package. The arrow on the retarder indicates the orientation of the fast axis (see below).

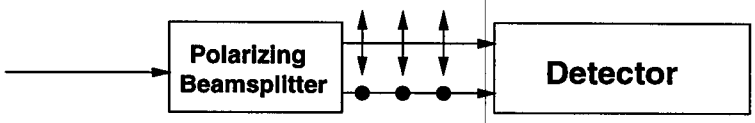

FIGURE 4. A simple (linear) polarimeter consisting of a polarizing beam-splitter that produces two displaced beams corresponding to orthogonal linear polarization states.

- to obtain equal modulation amplitudes in Q, U, and V, the retardation of the retarder should be close to $\delta = 127°$;
- Q and U are modulated at twice the frequency of V;
- the phase shift in modulation between Q and U is 90°, and the corresponding frequency is twice that of Stokes V, which requires measurements at 8 angles to determine all 4 Stokes parameters.

In the following, the modulation scheme employed by a polarimeter that measures Stokes parameters sequentially will be referred to as *temporal modulation.*

2.3.2. *Polarizing beam-splitter polarimeter*

Another simple polarimeter for linear polarization contains only a fixed polarizing beam-splitter that produces two beams corresponding to orthogonal polarization states (see Fig. 4). The full linear polarization information can be deduced by rotating the whole polarimeter assembly. In the following, we will refer to such an arrangement of simultaneous measurements of two (or more) Stokes parameters as *spatial modulation.*

2.3.3. *Comparison of temporal and spatial modulation schemes*

Temporal and spatial modulation schemes have different advantages and disadvantages. The most important ones are summarized in Table 2.

Since none of these schemes has clear advantages over the other, but the two schemes are rather complementary, modern, sensitive polarimeters often combine the two modulation schemes to combine the advantages and minimize the disadvantages. Such a combined approach is described in detail in Sect. 5.

2.4. *Statistical errors of polarization measurements*

When designing a polarimeter, it is important to model and understand the performance that can be expected. Once clear performance goals have been established, the design can be optimized to maximize the performance. The literature shows various ways to define and maximize the efficiency with which the polarization is measured, and it often depends on the exact polarimeter that is used, therefore making it difficult to directly compare the efficiency of various polarimeters.

Modulation Scheme	Advantages	Disadvantages
temporal	negligible effects of flat field and optical aberrations	influence of seeing if modulation is slow
	potentially high polarimetric sensitivity	read-out rate of regular array detectors limits modulation frequency
spatial	off-the-shelf array detectors can be used	requires up to four times larger array detector
	high photon collection efficiency	influence of flat field
	allows post-facto image reconstruction	influence of differential aberrations

TABLE 2. Comparison of spatial and temporal modulation schemes.

Errors in polarization measurements are typically separated into two components: statistical errors (mostly due to the photon statistics and detector read-out noise) and systematic errors (also called instrumental errors). When designing a polarimeter, a trade-off between the two error components needs to be made. For instance, it does not make sense to build a polarimeter that has very small systematic errors but so low an efficiency that the statistical errors completely dominate.

Making a few assumptions, we can derive the expected statistical noise in the Stokes parameters, which we will try to minimize. For this analysis, we can assume that:

- there is a linear relation between the Stokes parameters of the incoming light and the signals that are measured;
- the noise in the various measurements is independent;
- the noise has a Gaussian distribution.

For a large number of photons, which are needed for accurate polarimetry, a Gaussian distribution is a good approximation to the Poisson statistic that describes photon noise.

We combine the measured intensities into a signal vector $\boldsymbol{S}$, which is related to the incoming Stokes vector, $\boldsymbol{I}$ by the signal matrix X, where

$$\boldsymbol{S} = \mathsf{X}\boldsymbol{I} \,. \tag{2.19}$$

X is a 4 by m matrix where m is the number of intensity measurements that contribute to the polarization measurement. For example, $m = 4$ for most systems that use liquid crystals, while $m = 8$ for a rotating retarder approach as outlined above. X is a function of the free parameters in the polarimeter design. Since the polarimeter optics can be described by Mueller matrices, each row of X corresponds to the first row of the Mueller matrix describing the particular intensity measurement.

To determine the Stokes vector $\boldsymbol{I}$ from the measurements $\boldsymbol{S}$, X needs to be inverted. If

$$\mathsf{Y} = \mathsf{X}^{-1} \,, \tag{2.20}$$

or more generally for a non-square matrix using the Moore-Penrose generalized inverse (e.g. Albert 1972)

$$\mathsf{Y} = \left(\mathsf{X}^T\mathsf{X}\right)^{-1}\mathsf{X}^T \,, \tag{2.21}$$

then the standard deviations of the Stokes parameters, σ_{I_i}, are given by

$$\sigma_{I_i} = \sqrt{\sum_{j=1}^{4} \mathsf{Y}_{ij}^2 \sigma_{S_j}^2}\,, \tag{2.22}$$

where σ_{S_j} is the standard deviation of the intensity in measurement j. In most cases, σ_{S_j} does not depend on the measurement number j.

A more extensive treatment of statistical errors in polarimetry has been given by del Toro Iniesta and Collados (2000). When designing a polarimeter, we generally wish to minimize the standard deviations of the deduced Stokes parameters.

2.5. *Data reduction*

In order to achieve high polarimetric sensitivity, there will always be a substantial amount of data reduction involved. Often the raw data (before calibrations have been applied) have errors on the order of a few percent in the fractional polarization, while the expected signal is one or two orders of magnitude smaller. Typical reduction steps include:

- subtraction of dark current and bias;
- division by flat field;
- calculation of fractional polarization Q/I, U/I, and V/I;
- subtraction of polarization bias;
- removal of polarized fringes;
- calibration with polarization efficiency (polarization flat field);
- if required, multiplication with calibrated intensity I to obtain V, Q, and U.

To deduce the best data reduction strategy, one needs to understand the relevant instrumental effects so that they can be removed during processing. All data reduction steps should be based on a physical model of the data collection process, i.e. on a theory of the observing process and a model of the instrument. Once a theory is available, one can solve it for the parameters that should be determined as a function of the measured quantities. This solution will then also help in identifying the necessary calibration observations.

3. Optical components for spectropolarimetry

3.1. *Polarizers*

A polarizer is defined as an optical element that produces (at least partially) polarized light when the input light beam is unpolarized. Therefore, a polarizer can be linear, circular, or in general, elliptical, depending on the type of polarization that emerges.

There is a large variety of polarizers that all have their respective advantages and disadvantages. Here we will discuss the types of linear polarizers that are most often used in astronomical polarimetry.

3.1.1. *Jones and Mueller matrices for linear polarizers*

A linear polarizer can be described by its transmittance of the electrical field in two orthogonal directions. The Jones matrix for a linear polarizer is then given by

$$\mathsf{J}_p = \begin{pmatrix} p_x & 0 \\ 0 & p_y \end{pmatrix}\,, \tag{3.23}$$

where the real values $0 \leq p_x \leq 1$ and $0 \leq p_y \leq 1$ are the transmission factors for the x and y-components of the electrical field, i.e. $E'_x = p_x E_x$ and $E'_y = p_y E_y$. $p_x = 1, p_y = 0$

describes a linear polarizer in the $+Q$ direction, $p_x = 0, p_y = 1$ describes a linear polarizer in the $-Q$ direction, and $p_x = p_y$ describes a neutral density filter.

The corresponding Mueller matrix is given by

$$\mathsf{M}_p = \frac{1}{2}\begin{pmatrix} p_x^2 + p_y^2 & p_x^2 - p_y^2 & 0 & 0 \\ p_x^2 - p_y^2 & p_x^2 + p_y^2 & 0 & 0 \\ 0 & 0 & 2p_x p_y & 0 \\ 0 & 0 & 0 & 2p_x p_y \end{pmatrix} . \tag{3.24}$$

From this equation, it is evident that an unpolarized incoming beam will always be linearly polarized. However, the emerging Stokes vector does not correspond to a completely polarized beam unless $p_x = 0$ or $p_y = 0$. If the polarizer only produces a partially polarized beam from unpolarized light, it is called a *partial* linear polarizer. Any real polarizer is always only a partial polarizer.

If the incoming beam is polarized, the emerging beam is, in general, elliptically polarized, even for a purely linear polarizer because of the non-zero diagonal terms $2p_x p_y$ in the Mueller matrix. A totally polarized beam will remain totally polarized even when passing an ideal partial linear polarizer, i.e. an ideal polarizer does not depolarize. However, real polarizers can produce minute amounts of unpolarized light from a fully polarized beam because of scattering within the polarizer. Nevertheless, this effect is small and can almost always be neglected.

When characterizing the quality of actual linear polarizers, two different parameters are used to describe the performance. k_1 describes the (intensity) transmittance of the polarizer for a fully linearly polarized beam whose angle is chosen such as to maximize the transmitted intensity. k_2 is the minimum transmittance as a function of the angle of the incoming linearly polarized beam. It is evident that $k_1 = p_x^2$ and $k_2 = p_y^2$ if we assume that $p_x > p_y$. The ratio of k_1 to k_2 is called the *extinction ratio*. k_1 and k_2 are often tabulated for various polarizers as a function of wavelength and can be determined from the transmittances for unpolarized light of parallel and crossed identical polarizers, which are given by

$$\begin{aligned} T_{\text{parallel}} &= \tfrac{1}{2}\left(k_1^2 + k_2^2\right) \\ T_{\text{crossed}} &= k_1 k_2 \end{aligned} . \tag{3.25}$$

Finally, the Mueller matrix for a total linear polarizer at position angle θ is given by

$$\mathsf{M}_{\mathrm{p}}(\theta) = \frac{1}{2}\begin{pmatrix} 1 & \cos 2\theta & \sin 2\theta & 0 \\ \cos 2\theta & \cos^2 2\theta & \sin 2\theta \cos 2\theta & 0 \\ \sin 2\theta & \sin 2\theta \cos 2\theta & \sin^2 2\theta & 0 \\ 0 & 0 & 0 & 0 \end{pmatrix} . \tag{3.26}$$

3.1.2. *Wire grid polarizers*

Grids of parallel conducting wires with a spacing d of the order of the wavelength λ of the light act as a polarizer. Intuitively, one might expect that the electric field parallel to the wires is transmitted because it 'slips' through the wires. On the contrary, it is the plane of polarization perpendicular to the wires that is transmitted because the electric field component (of the electromagnetic wave) parallel to the wires induces electrical currents in the wires, which strongly attenuates the transmitted electric field parallel to the wires. The induced electrical current is such that the polarization parallel to the wires is reflected. It is thus possible to produce a polarizing beam-splitter with a wire grid polarizer, which reflects and transmits orthogonal linear polarization states. As a rule of thumb, if $d < \lambda/2$, then the polarization is strong. If $d >> \lambda$, then the transmission

of both polarization states is high, and thus the polarization of the transmitted beam is weak.

Wire grid polarizers were first used by Heinrich Hertz at radio wavelengths. They are used mostly in the infrared because the wire spacing becomes very small at visible wavelengths. Modern commercial wire grid polarizers are made by depositing a thin-film metallic grid pattern on a suitable infrared substrate. They are available for wavelengths larger than 1 μm. For longer wavelengths where appropriate substrates are not available, free-standing wire grid polarizers are employed.

3.1.3. *Polarcor*

Available since 1984, Polarcor made by Corning is a glass polarizer with high performance between 633 and 1550 nm. It is made from a borosilicate glass containing silver particles aligned along a common axis. The elongated, conducting silver particles act as small wires. Polarization occurs within 25 to 50 μm of each surface. In the UltraThin version, polarization occurs throughout the entire body of the glass. Unfortunately, the maximum diameter of Polarcor is currently limited to 30 mm.

3.1.4. *Dichroic crystals*

Dichroic materials preferentially absorb one polarization state. The behavior depends on the wavelength, i.e. the materials appear to have different colors depending on the angles of illumination and viewing. Dichroism arises from the anisotropy of the complex index of refraction (see Landi Degl'Innocenti in this volume). Examples of naturally occurring dichroic crystals are tourmaline and herapathite. In 1852, W.B. Herapath discovered a salt of quinine that had polarizing properties. He succeeded in making artificial crystals large enough to study under a microscope. Di-iodosulphate of quinine is now known as herapathite. However, it is generally difficult to produce uniform, large dichroic crystals, which is why this type of polarizer is only of historical interest.

3.1.5. *Polaroid-type polarizers*

In 1928, Edwin Land made a suspension of tiny herapathite crystals, which he spread as a thin layer between supporting sheets. The crystals also have a magnetic dipole moment, so that if a suspension is placed in a very strong magnetic field, they become oriented to form a uniform dichroic layer. If the aligned crystals are suspended in a polymer, they set. Land called this a J-type polarizer. However, this first type of sheet polarizer had problems with the finite lifetime because the crystals become disoriented over time.

The next-generation sheet polarizer, also invented by Edwin Land in 1938, is based on molecular dichroism. H-type sheet polarizers are made by heating and stretching a sheet of polyvynil alcohol (PVA) that is laminated to a supporting sheet of cellulose acetate butyrate. The PVA is then treated with an iodine solution. The difference between various H-type polarizers is in the amount of iodine absorbed by the PVA. The PVA-iodine complex is analogous to a short, conducting wire. This is the operating principle of H-type polarizers, which are still in use today. Of course, the axis of maximum transmission for linearly polarized light is perpendicular to the stretch direction. The commercial names for Polaroid sheet polarizers such as HN-38 identify the overall type (H), the color (N=neutral) and the approximate transmittance of a single polarizer for unpolarized light (38%).

Other types of Polaroid sheet polarizers include the K-type, which is close in performance to H-type polarizers but more stable under extreme environmental influences such as temperature and humidity. Again, PVA is the starting material, but this time

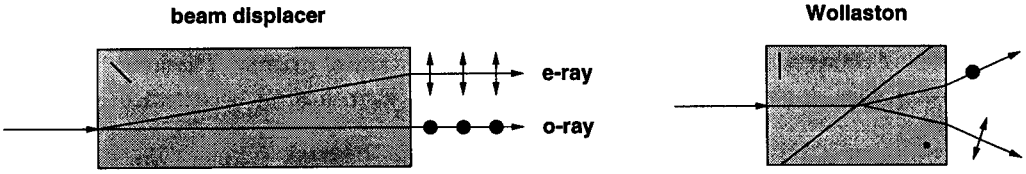

FIGURE 5. Beam displacers and Wollaston prisms are often used in astronomical polarimeters. A simple block of calcite with the optic axis at about 45° (indicated by the short line) splits a single ray into two parallel rays of opposite linear polarization. In the Wollaston, two calcite or quartz prisms with their optic axes at 0° and 90° deflect the two linear polarizations symmetrically.

hydrogen and oxygen atoms are removed by a chemical process to produce polyvinylene from some of the PVA molecules, and stretching aligns the long chain molecules.

Finally HR-type polarizers, developed at Polaroid between 1943 and 1951 by Blake, are based on a PVA-polyvinylene-iodine complex that works well from 0.7 to 2.3 μm.

The very thin polarizer material is laminated between sheets of plastic or glass. The plastic sheeting can be removed with organic solvents to obtain the polarizing foil alone.

3.1.6. *Crystal-based polarizers*

Crystals can have different indices of refraction for each axis:

$$n_x \neq n_y \neq n_z \ . \tag{3.27}$$

Uniaxial crystals axis have only one axis that has a different index of refraction as compared to the other two axes:

$$n_x \neq n_y = n_z \ . \tag{3.28}$$

The *optic axis* of a uniaxial crystal is the axis that has a different index of refraction. The *fast axis* is the axis with the smallest index of refraction since the speed of light along that axis is the fastest. When sending a ray of light through a uniaxial crystal, the single ray is generally split into two rays. The *ordinary ray* (or short *o-ray*) passes the crystal without any deviation, while the *extraordinary ray* (or *e-ray*) is deviated at the air-crystal interface. The two emerging rays have orthogonal polarization states. It is common to use the indices of refraction for the ordinary ray (n_o) and the extraordinary ray (n_e) instead of the indices of refraction in the crystal coordinate system.

It is outside of the scope of this chapter to deal with the optical calculations of crystals, which are rather complicated, even for uniaxial crystals. However, we will present some of the most important results here. An introduction to uniaxial crystal optics is given in Collett (1993). A more advanced treatment of crystal optics that is easy to read has been given by Wahlstrohm (1960).

The polarizing beam displacer or beam-splitter is the most simple crystal polarizer. It consists of a single block of calcite (or other uniaxial crystal with large birefringence) with the optic axis at about 45°. On the interface between air and calcite, the extraordinary ray is deflected while the ordinary ray just passes through (see Fig. 5). For calcite, the splitting is about 0.095 times the thickness. The two emerging rays are parallel and have orthogonal linear polarization states.

The Nicol prism, invented in 1828 by William Nicol was the first actual polarizer based on crystals. However, it has been superseded by considerably better designs (discussed below). It consists of two calcite prisms that are held together by Canada balsam. The angles are chosen such that the ordinary ray undergoes total internal reflection on the interface between the calcite and the Canada balsam.

Glan-Thompson polarizers also consist of two calcite prisms that are cemented together. The ordinary beam undergoes total internal reflection and is absorbed by black

paint on the side of one of the prisms. There are two versions that differ in their prism angles and the index of refraction of the cement between the two crystal prisms. The long version has an acceptance angle of about 25°, while the short form has an acceptance angle of about 15°.

Glan or Glan-Foucault polarizers consist of two prisms made of calcite that are separated by an air gap. As all the other crystal-based polarizers, it is usable from about 300 nm to 2700 nm, but absorption of the deflected beam occurs above 2 μm. The field of view is between 13° and 7.5°, but this acceptance angle is rotationally symmetrical only at a single wavelength. Again, total internal reflection of the ordinary ray is responsible for the polarization. The transmission is not as high as for the Glan-Thompson polarizer because of reflection losses at the internal calcite-air interfaces.

Wollaston prisms are similar to beam displacers since they also produce two beams with orthogonal linear polarizations. However, Wollaston prisms do not displace the two beams but deviate them in opposite directions (see Fig. 5). They are made of calcite or quartz prisms with perpendicular optical axes that are cemented together. The usable spectral range is typically 300 nm to 2200 nm, the upper limit being given by the absorption of the ordinary beam. The polarization directions are parallel and vertical to the refracting edge. The e-ray in the first prism becomes the o-ray in the second prism and is bent toward the normal. The o-ray in the first prism becomes the e-ray in the second prism and is bent away from the normal. The angle of divergence is determined by the wedge angle, which is typically between 15° and 45°.

3.1.7. *Brewster-angle polarizers*

When calculating the polarization of reflected and transmitted beams for an air-dielectric interface as a function of angle of incidence (see the chapter by Landi Degl'Innocenti), it becomes evident that there is an angle α_B, the Brewster angle, at which the reflected beam is completely polarized. This angle has a simple relation with respect to the index of refraction n of the dielectric:

$$\tan \alpha_B = n \,. \tag{3.29}$$

However, the reflected intensity is rather small such that a polarizer based on the Brewster-angle reflection is not very effective at the wavelengths considered here. However, the transmitted beam is somewhat polarized, and the transmittance for that polarization state is 100%. A stack of dielectric plates can therefore be used as a polarizer with good transmittance.

3.1.8. *Thin-film polarizers*

Thin-film polarizers are mostly used in the form of cube beam-splitters where the two orthogonally polarized beams emerge at right angles. Polarizing cube beam-splitters are based on a thin film stack on the inside of two glass prisms that are cemented together such that total internal reflection occurs at the Brewster angle within the thin film. This type of polarizer has a limited extinction ratio and wavelength range, but it can be manufactured relatively cheaply even at large apertures (5–10 cm). Thin-film stacks that act as polarizers can also be deposited on oblique plates from which the polarized beam is reflected.

3.1.9. *Comparison of polarizers*

Table 3 summarizes the properties of polarizers that are typically used in astronomy. Crystal-based polarizers are expensive and typically limited in aperture to about 40 mm. Polaroid sheet polarizers are less transparent and do not have as high an extinction ratio, but they are available in sizes up to about 50 cm and are cheap.

type	extinction ratio	transmission (polarized)	wavelength range (nm)	bandpass (nm)	acceptance angle (°)
Glan	$> 10^5$	> 84%	300-2700	full	8
Glan-Thompson	$> 10^6$	> 92%	300-2700	full	15-25
Wollaston	$> 10^6$	> 92%	300-2200	full	20
Polarcor	$> 10^4$	> 80%	633-1550	150	> 20
Polaroid	$150 - 10^4$	> 75%	310-2000	200	> 20
Polarizing cube	> 500	> 90%	400-1600	200-400	10
Wire Grid	> 100	> 90%	$10^3 - 10^6$		> 20

TABLE 3. Comparison of various types of polarizers that are used in astronomy.

3.2. *Fixed linear retarders*

A retarder is an optical element that splits an incoming beam into two components, retards the phase of one of these components, and reunites the components at the exit into a single beam. An ideal retarder does not change the intensity of the light, nor does it change the degree of polarization. Any retarder can be characterized by the two (not identical) Stokes vectors of incoming light that are not changed by the retarder. These two Stokes vectors are sometimes called the *eigenvectors* of the retarder. Depending on whether these Stokes vectors describe linear, circular, or elliptical polarization, the retarder is called a linear, circular, or elliptical retarder. In the following, we will only consider linear retarders because they are by far the most common type of retarder.

3.2.1. *Mueller and Jones matrices for linear retarders*

A linear retarder with its fast axis at 0° is characterized by a Jones matrix of the form

$$\mathsf{J}_r(\delta) = \begin{pmatrix} e^{i\frac{\delta}{2}} & 0 \\ 0 & e^{-i\frac{\delta}{2}} \end{pmatrix}, \tag{3.30}$$

where δ is the phase shift between the two linear polarization components expressed in radians. Since the absolute phase does not matter, it is possible to write the Jones matrix of a retarder with the retardation in only one matrix element. However, it is advisable to use the 'symmetric' version given above because it avoids introducing an absolute phase that depends on the retardation. Use of the 'asymmetric' version has led to some erroneous theoretical calculations of the instrumental Mueller matrix of telescopes.

The corresponding Mueller matrix is given by

$$\mathsf{M}_r = \begin{pmatrix} 1 & 0 & 0 & 0 \\ 0 & 1 & 0 & 0 \\ 0 & 0 & \cos\delta & -\sin\delta \\ 0 & 0 & \sin\delta & \cos\delta \end{pmatrix}. \tag{3.31}$$

It is important to realize that the combination of two or more linear retarders in series will, in general, not be equivalent to a linear retarder, but be equivalent to a single elliptical retarder.

3.2.2. *Zero and multiple order linear retarders*

Most retarders are based on birefringent materials that have different indices of refraction for different angles of the incoming linear polarization. Typical birefringent materials that are used are quartz, mica, and polymer films with oriented molecules.

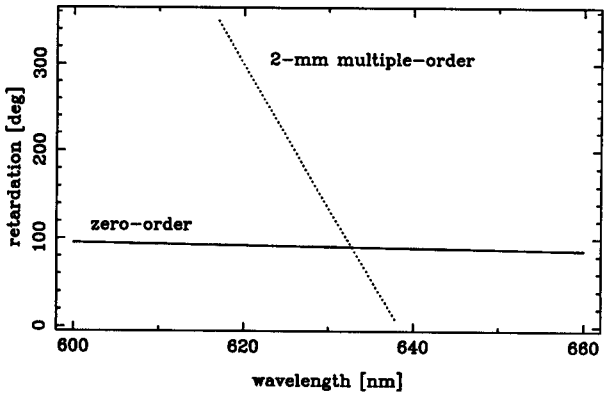

FIGURE 6. Wavelength dependence of a 2-mm multi-order and a true zero-order quartz quarter-wave retarder.

The retardation (delay between ordinary and extraordinary ray) is given by

$$N\lambda = d\,(n_e - n_o)\ , \tag{3.32}$$

where d is the geometrical thickness, λ is the wavelength, and n_e and n_o are the indices of refraction for the extraordinary and the ordinary rays, respectively. N is the retardation expressed in waves. A quarter-wave plate is obtained with $N = m + \frac{1}{4}$ and m being an integer. If $m = 0$, we call it a *true zero-order* retarder. If $m > 0$, we call it a *multi-order* retarder.

Of course, a retardation of 1.25 waves has the same effect on polarization as a retardation of 0.25 waves. However, it is evident that the thicker the retarder becomes (larger d), the faster the retardation changes as a function of wavelength, even if the indices of refraction n_o and n_e would not depend on the wavelength (see Fig. 6).

3.2.3. *Crystal retarders*

Quartz is available in fairly large sizes and can be produced artificially. It is therefore the most commonly used crystal material for high-quality retarders. A true zero-order quarter-wave retarder in the visible is about 15 μm thick. While such true zero-order quartz retarders can now be fabricated on glass substrates, the usual way to obtain a (so-called *compound*) zero-order retarder consists in combining two approximately 1-mm thick plates cut parallel to the optic axis with a difference in thickness that corresponds to the path difference of a true zero-order retarder. The two plates are optically contacted with their fast axes at 90° with respect to each other. The retardation of the two plates therefore cancels except for the small path-length difference. The usable spectral range of quartz retarders is from about 180 nm to 2700 nm. For wavelengths below 230 nm, the plates are manufactured from synthetic crystal quartz.

Mica is another material that is often used for commercial retarders. It is cheap and available in large sizes (20 cm by 20 cm). Mica crystals can easily be cleaved into very thin sheets of appropriate thickness to obtain true zero-order retarders. A quarter-wave plate in the visible is about 50 μm thick. Mica is transparent from about 350 nm to 6 μm, but it absorbs even in the visible. Since the required thickness at longer wavelengths, and therefore the absorption, become rather large, mica retarders are normally not used for wavelengths larger than about 1.6 μm.

Other crystals that are used for manufacturing retarders include MgF_2, which transmits over a large wavelength range from the ultraviolet to the mid-infrared and stressed LiF for wavelengths around 100 nm.

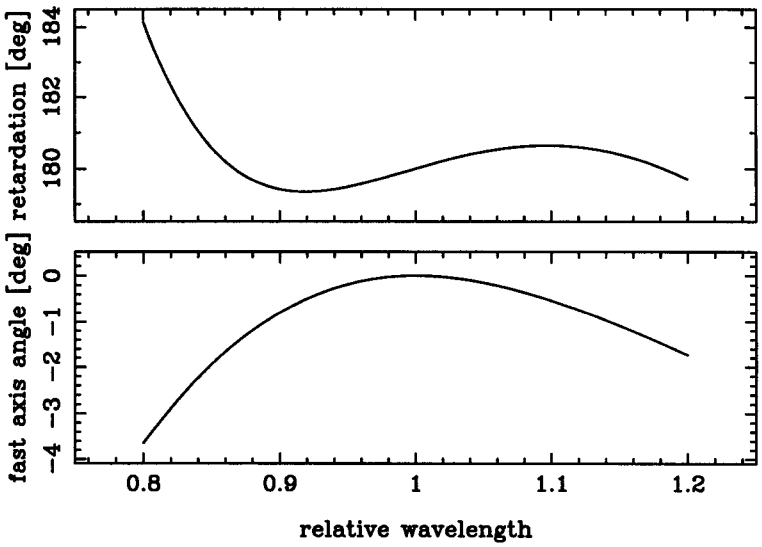

FIGURE 7. Theoretical variation of retardation and fast axis orientation as a function of relative wavelength for a Pancharatnam achromatic half-wave plate.

3.2.4. *Polymer retarders*

Stretched polymers (e.g. polyvinyl alcohol) are also birefringent. The fast axis is perpendicular to the stretch direction. They were invented by Land, West, and Makas around 1946. The thickness of a quarter-wave retarder is about 20 μm in the visible. Polymer retarders are true zero-order retarders that are highly transparent even in the ultraviolet. For certain retardance values, polymer retarders in sizes of up to 40 cm can be obtained.

3.2.5. *Achromatic retarders*

As seen above, retarders are highly wavelength sensitive. By combining two materials with opposite variations of $\delta n = n_e - n_o$ with wavelength, and by choosing appropriate thicknesses, an achromatic retarder can be built whose retardance is correct at two wavelengths. The most used combination of materials is quartz and MgF_2. The useful wavelength range of this type of achromatic retarders is about 50% of the central wavelength.

Another approach uses three identical retarders. Invented by Pancharatnam (1955) for half-wave plates, the outer plates have parallel fast axes, while the fast axis of the inner plate is rotated by about 60°. In contrast to the achromatic wave-plates discussed above, the fast axis direction of the combined retarder depends on the wavelength. Figure 7 shows the variation of the retardation and the fast axis direction as a function of wavelength. Achromatic quarter-wave plates can be constructed in a similar way, although the performance is not as good as for the half-wave retarders.

By combining three identical crystal achromatic retarders with the Pancharatnam approach, superachromatic half-wave plates can be constructed. Again, the fast axis direction depends on the wavelength. However, the angular acceptance angle is very limited because of the thickness of the combined 6 plates (see below). The useful wavelength range for commercially available superachromatic waveplates extends from about 300 nm to 1100 nm.

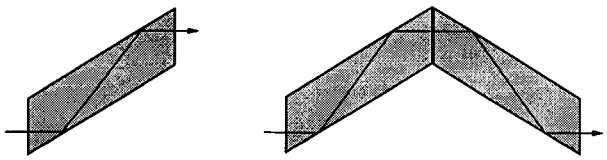

FIGURE 8. Traditional arrangements for quarter-wave (left) and half-wave (right) Fresnel rhombs.

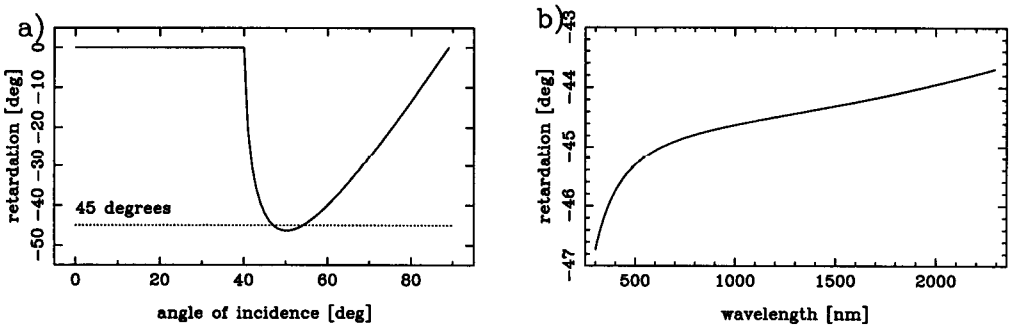

FIGURE 9. Variation of retardance on total internal reflection with a) angle at 632.8 nm and b) wavelength at 55.08° for a BK7 and air interface.

3.2.6. *Fresnel rhombs*

Another approach for obtaining achromatic retarders makes use of the phase shift on total internal reflection on an interface between dielectrica. Reflections on dielectric interfaces do not produce a phase shift (or retardance) except for total internal reflection. Retarders using total internal reflection are typically called *Fresnel* rhombs. When working in the visible, it is normally not possible to achieve a 90° phase shift on a single reflection. However, a single total internal reflection can be arranged such that a retardation of $\lambda/8 = 45°$ is achieved. Two (suitably aligned) reflections therefore provide a retardation of $\lambda/4$, and a half-wave retardation can be achieved with four total internal reflections. Figure 8 shows two possible arrangements for quarter- and half-wave Fresnel rhombs. Historically, this was the first type of retarder that was developed (by Fresnel).

The requirement for total internal reflection on a glass-air interface is

$$n_i \sin\beta > 1\,, \tag{3.33}$$

where n_i is the index of refraction of the glass and β is the (internal) angle of incidence. The phase shift is given by

$$\tan\delta/2 = -\frac{\cos\beta\sqrt{n_i^2\sin^2\beta - 1}}{n_i \sin^2\beta}\,. \tag{3.34}$$

For BK7, the most common type of optical glass, at a wavelength of 632.8 nm (HeNe laser wavelength) the index of refraction is 1.5151, and at an angle of incidence of 55.08°, the retardation is 45° (or $\lambda/8$). Figure 9a shows the variation of the retardation with the angle of incidence. Below an angle of incidence of 41.3°, no internal reflection occurs. The retardation strongly depends on the angle of incidence. Therefore, Fresnel rhombs have only a small acceptance angle. A deviation of ±0.5° from normal incidence changes the retardation by ±0.5%.

For a material with an index of refraction of 1.5538, an angle of incidence of 45.0° produces exactly a 45° phase retardation. Two right-angle prisms with total internal

type	retardance accuracy (%)	wavelength range (nm)	bandpass (nm)	acceptance angle (°)
quartz	0.4	180-2700	100	3
MgF_2	0.4	140-6200	100	3
mica	4	350-1550	100	10
polymer	0.6	400-1800	100	10
Fresnel	2	240-2000	330-1000	2

TABLE 4. Comparison of various types of commercially available zero-order retarders that are used in astronomy. For quartz and MgF_2, it is assumed that they are compound zero-order retarders. The accuracy in percent refers to a half-wave plate.

reflection form a quarter-wave plate. When using right-angle prisms for beam deflection, one needs to keep in mind that they act as significant retarders.

The variation of the retardance with wavelength is purely due to the variation of the index of refraction with wavelength, which is generally small. Therefore, Fresnel rhombs are very achromatic. Figure 9b shows the theoretically calculated variation of the retardance for a single total internal reflection for BK7 at 55.08° from 300 nm to 2300 nm. The performance of Fresnel rhombs with respect to the angle of incidence and the variation of the retardance with wavelength can be improved by coating the reflecting surfaces with thin films.

3.2.7. *Comparison of zero-order retarders*

Table 4 summarizes the properties of commercially available zero-order retarders that are typically used in astronomy. Mica and polymer retarders can be produced with fairly large apertures, however, the retardance accuracy tends to be reduced for larger apertures. Both mica and polymer retarders have the advantage of large acceptance angles because they are true zero-order retarders. Crystal-based retarders are limited in aperture size. Fresnel rhombs are the only achromatic retarders consisting of a single piece of optics, but have a very limited acceptance angle.

3.3. *Variable retarders*

For building sensitive polarimeters, it is often desirable to have retarders whose retardance can be varied quickly. This can be achieved either by changing the birefringence (liquid crystals, Kerr and Pockels cells, photoelastic modulators) or by changing the geometrical thickness (e.g. Soleil compensators). Since the latter is necessarily associated with a mechanical motion, it is normally not used for polarimeters and will therefore not be discussed any further.

3.3.1. *Nematic liquid crystal retarders*

Liquid crystals are fluids whose molecules are elongated. At high temperatures, the liquid crystal is isotropic. In the *nematic phase*, the molecules are randomly positioned but aligned essentially in one direction. Some liquid crystals line up parallel or perpendicular to an outside electrical field. For these, the dielectric constant anisotropy is often large, making the liquid crystal very responsive to changes in the applied electric field. The birefringence δn can be very large (larger than typical crystal birefringence). Sheets of liquid crystal can therefore behave like an electronically adjustable optical retarder. The liquid crystal layer is only a few μm thick and represents a true zero-order retarder.

The anisotropy of liquid crystals, and therefore also their birefringence, shows a strong

temperature dependence. With zero voltage applied externally, the liquid crystal molecules are parallel to the substrates due to an alignment layer, therefore maximizing the retardation. With an electrical field applied, the liquid crystal molecules tip perpendicular to the substrate causing a reduction in the effective birefringence and hence, the retardation. The alignment layer between the substrate and the liquid crystal prevents the molecules at the surface to rotate freely. This causes a residual retardance of about 30 nm even at high voltages (about 20 V). The retardance changes by about -0.4% per °C. The response time of nematic liquid crystal retarders is proportional to the square of the layer thickness (=total retardance) and of the order of 20 ms.

3.3.2. *Ferro-electric liquid crystal retarders*

The *smectic* liquid crystal phases are characterized by well-defined layers that can slide over one another. The molecules are positionally ordered along one direction. In the smectic C phase, the molecules are tilted away from the layer normal. *Ferroelectric liquid crystals* (FLCs) are the tilted phases of chiral molecules (called smectic C*), which have a permanent polarization, which is why they are called ferroelectric. They respond much more quickly to externally applied fields than nematic liquid crystals and can be used to make fast, bistable electro-optic devices when placed between closely-spaced, electrically conducting glass plates. FLC variable retarders act like retarders with a fixed retardation where the direction of the fast axis can be switched by about 45° (switching angle) by alternating the sign of the applied electrical field. They are true zero-order retarders with switching times on the order of 150 μs. The switching angle is rather temperature sensitive, while the retardance tends to be rather insensitive to temperature variations.

3.3.3. *Photoelastic modulators (PEMs)*

Isotrop and uniform optical materials such as glass become birefringent when strain (e.g. due to compression) is applied in one axis. This is commonly referred to as stress-induced birefringence and the effect is called piezo-optical or photo-elastic effect. For example, a block of a few cm in side length of common BK7 glass can be stressed enough by hand such as to introduce a quarter-wave retardation.

The stress-induced birefringence is proportional to the strain σ. The retardation in waves is therefore given by

$$\delta = \frac{1}{\lambda} C d \sigma \,, \tag{3.35}$$

where C is the stress optical constant, d is the thickness of the variable retarder, and λ is the wavelength. It is possible to construct variable retarders by just adequately compressing optical glass. However, one needs to apply considerable mechanical power to modulate the stress-induced birefringence.

One way to obtain a birefringence modulation with much reduced power is to use a mechanically resonant oscillation since the required mechanical power is proportional to one over the mechanical Q, which is on the order of 10^3 to 10^4 for most glasses.

If a slab of length L is excited at its fundamental mode, a standing acoustic wave with a wavelength of $2L$ is produced. The frequency of the oscillation is given by

$$\omega = \frac{c_s}{2L} \,, \tag{3.36}$$

where c_s is the sound speed in the optical material. For a 57-mm-long fused silica slab, the resonance frequency is 50 kHz.

It is easy to calculate the resulting stress and hence the retardance as a function of

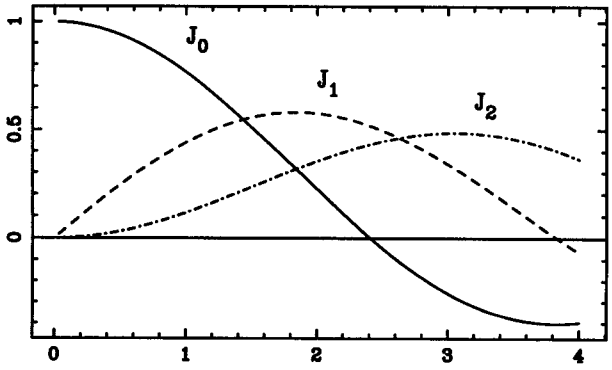

FIGURE 10. Bessel functions of order 0, 1, and 2.

position x and time t. The stress-induced birefringence $\delta(x,t)$ is given by

$$\delta(x,t) = A \sin\omega t \sin(\frac{\pi x}{L}) , \tag{3.37}$$

where A is the amplitude of the oscillation and x extends from 0 to L.

To make the slab oscillate, a quartz crystal with electrodes on its surfaces is forced to oscillate by an externally applied electrical field via the piezo effect. The quartz slab is mechanically coupled to the modulator slab, and the electrical field is driven at the mechanical resonance frequency. The oscillation amplitude A can be regulated with an electronic feedback circuit.

The oscillation is dampened by friction losses within the modulator material. Since the energy loss is inversely proportional to the mechanical Q, and since Q is very large, the energy loss in the modulator is not critical, and the required drive power is small (0.1 to 1 W). A material with a high Q such as fused silica ($Q \approx 10^4$) is desirable. Typical glass has a Q of about 10^3 and is therefore less often used. It is interesting to note that the required drive power does not depend on the length of the slab.

By grouping the $\sin(\frac{\pi x}{L})$ term and the amplitude A into a spatially varying amplitude $A(x)$, the birefringence can be rewritten as

$$\delta(x,t) = A(x)\sin(\omega t) . \tag{3.38}$$

The PEM represents a true zero-order retarder. Its Mueller matrix corresponds to a retarder with a time dependent retardation and therefore contains elements with $\sin\delta(x,t)$ and $\cos\delta(x,t)$. By expanding $\sin(\sin(\cdot))$ and $\cos(\sin(\cdot))$ terms into Bessel functions, the Mueller matrix elements become

$$\sin\delta(\mathrm{x,t}) = 2J_1(A(x))\sin\omega t + \cdots , \tag{3.39}$$

$$\cos\delta(x,t) = J_0(A(x)) + 2J_2(A(x))\cos 2\omega t + \cdots , \tag{3.40}$$

$$\tag{3.41}$$

where $J_{0,1,2}$ are the Bessel functions of order 0,1 and 2 (see Fig. 10).

PEMs are stable in operation, show no degrading at high intensity levels and/or UV irradiation, have good optical properties, a large spatial and angular aperture, and require only low voltages at moderate driving powers of less than 1 W. The disadvantages are the sinusoidal modulation (as compared to the more efficient square-wave modulation that can be achieved with liquid crystals) and the very high modulation frequency of 20 to 50 kHz, which requires specialized array detectors (see below).

Modulation Scheme	Advantages	Disadvantages
rotating retarder	high stability	relatively slow modulation
	large wavelength range	beam motion
		needs 8 measurements for all Stokes parameters
liquid crystals	relatively fast modulation	narrow simultaneous wavelength range
	only 4 measurements for all Stokes parameters	limited temporal stability
	no moving parts	damaged by strong UV light
PEM	very fast modulation	narrow simultaneous wavelength range
	high stability	needs special CCD camera
	no moving parts	spatial retardance variation

TABLE 5. Comparison of various temporal modulation schemes employed in astronomical spectropolarimeters.

3.3.4. *Pockels and Kerr cells*

Anisotropy in an otherwise isotropic material can also be introduced by an externally applied electrical field. The material then behaves like a uniaxial crystal. This effect was discovered by John Kerr in 1875 using glass and a high voltage electrical field. This effect also occurs in liquids and some gases. The birefringence induced by the Kerr effect is proportional to the square of the electric field. The latter implies that high voltages are required for Kerr cells.

F.R. Pockels discovered that an electrical field applied along the line of sight and parallel to the crystal optic axis produces birefringence that is proportional to the applied electrical field. Therefore, Pockels cells do not require high voltages. Since crystals are required for Pockels cells, the aperture of commercially available cells is typically limited to about 7 cm. The world's largest Pockels cells of 40 cm by 40 cm clear aperture are currently being developed for the National Ignition Facility, but the technology that is used to bring the electrical current to the crystal faces is not useful for astronomy.

3.4. *Comparison of modulation schemes*

Now that we have reviewed all the ingredients of typical astronomical polarimeters, we can compare different polarimeter concepts employing temporal modulation schemes. Table 5 compares three different approaches. The rotating retarder approach is common in both night-time and solar polarimeters. A large simultaneous wavelength range can be observed simultaneously by using superachromatic waveplates or Fresnel rhombs. While variable retarders avoid many of the problems of the rotating waveplate approach, they are typically limited to a narrow spectral range because of the current absence of achromatic variable retarders.

Achromatic variable retarders would provide a major new addition to astronomical polarimetry because they would have all the advantages of current variable retarders but could be used over a large, simultaneous wavelength range. Achromatic retarders using two different materials are not useful because each of the materials needs to have a

retardance of many waves, which cannot be achieved with any of the variable retarders available today. The Pancharatnam approach looks more feasible. However, variable retarders that rely on a change in birefringence (such as nematic liquid crystals and PEMs) will not work because the way the Pancharatnam approach works, which minimizes the overall retardance dependence on the retardance of the individual components. However, three half-wave FLCs in a Pancharatnam configuration should provide an excellent achromatic half-wave plate whose fast axis can be switched by 45°. Such a device has not yet been built to my knowledge.

4. Instrumental errors

It might seem excessive to devote a whole section to instrumental errors in spectropolarimeters. However, astronomical spectropolarimetry is often limited by systematic instrumental errors rather than by statistical errors such as photon and read-out noise, in particular in highly sensitive solar observations.

The following instrumental errors are commonly encountered in high-precision spectropolarimetry:

- Atmospheric seeing and guiding errors
- Instrumental polarization due to
  - Telescope and instrument optics
  - Polarized scattered light in telescope and instrument
  - Spectrograph slit polarization
  - Angle, wavelength, and temperature dependence of retarders and polarizers
  - Crystal aberrations
  - Polarized fringes
- Ghost images
- Variable sky background
- Unpolarized scattered light in atmosphere and optics
- Limited calibration accuracy

In the following, we will not discuss the influence of gratings on polarization because that is a rather complicated issue outside the scope of this chapter. In general, low-order gratings exhibit large variations of the polarization with wavelength. At some wavelengths, they often act as complete polarizers. Maximum transmission is normally obtained with the polarization parallel to the grating lines. High-order echelle gratings typically have only a minor influence on the polarization.

Finally, there will also be some systematic errors due to the data reduction. We will deal with the most important of these error sources in detail in the following sections.

In many cases the instrumental effects due to the telescope and the instrument can be described by Mueller matrices, which have the general form

$$\begin{pmatrix} I\rightarrow I & Q\rightarrow I & U\rightarrow I & V\rightarrow I \\ I\rightarrow Q & Q\rightarrow Q & U\rightarrow Q & V\rightarrow Q \\ I\rightarrow U & Q\rightarrow U & U\rightarrow U & V\rightarrow U \\ I\rightarrow V & Q\rightarrow V & U\rightarrow V & V\rightarrow V \end{pmatrix} . \tag{4.42}$$

The various terms are grouped into three categories:

- $I \rightarrow X, X = Q, U, V$: instrumentally induced *polarization*
- $X_1 \rightarrow X_{2\neq 1}$ and $X \rightarrow I$: instrumentally introduced *cross-talk*
- $X \rightarrow X$: instrumentally introduced *depolarization*

4.1. *Seeing and guiding errors*

Fortunately, air is not birefringent. Therefore, seeing does not produce polarization per se. However, whenever polarization measurements are not carried out simultaneously, seeing can introduce spurious polarization signals because sequentially recorded images will be differently distorted by seeing. The same holds for telescope guiding errors. Therefore, sequential polarization measurements should be modulated at a frequency that is faster than typical seeing frequencies, which are on the order of a few hundred Hz. To completely avoid this issue, measurements should be carried out simultaneously.

4.2. *Polarizing telescopes*

Every telescope introduces some polarization, although the amount may be very small. Rotationally symmetric telescopes are often called *polarization-free* because, theoretically, they would not introduce any net polarization at the very center of the field of view, although they do introduce a very small amount of depolarization. For points away from the center, even a rotationally symmetric telescope will introduce polarization (e.g. Sen & Kakati 1997). Furthermore, seeing destroys the rotational symmetry even in the center of the field of view (Sánchez Almeida 1994). Therefore no telescope should be considered to be completely free of instrumental polarization.

4.2.1. *Stress induced birefringence in glass*

Every piece of glass has some remaining internal stress from the manufacturing process. While these stresses can be minimized by extended annealing periods during the manufacturing, there will always be some remaining stress, which introduces birefringence. As a rule of thumb, one should expect about 5 nm of birefringence for every cm of high-quality glass thickness. In the visible, this will lead to a cross-talk of about 1% between V and Q, U for every cm of glass.

Apart from these static stresses, there is also temperature-induced stress that leads to a time-dependent birefringence. Temperature gradients in glass lead to stresses due to the varying thermal expansion. A careful choice of the type of glass can often alleviate this problem. For instance, fused silica is 12 times better than BK7 as far as temperature-induced birefringence is concerned. Temperature gradients also introduce optical aberrations because of the temperature dependence of the index of refraction. A correlation between birefringence and optical aberrations will lead to different PSFs for different Stokes parameters, which can amount to up to a few percent for diffraction-limited imaging. However, in the following, we will always assume that the observations are averaged over the PSF, i.e. the observations are not diffraction-limited.

4.2.2. *Oblique transmission and reflection*

Oblique reflections off and transmission through optical surfaces such as mirrors introduce polarization and cross-talk between the Stokes parameters. Transmission through dielectric materials such as glass introduces retardation, but no polarization. Oblique reflections on mirrors do not only occur on solar telescopes that have often complicated mirror, but they also occur in night-time telescopes, e.g. in Nasmyth and Coudé foci. The accurate modeling of these reflections is not easy because of oxide and sometimes oil layers on the mirrors and their associated interference effects. Similar issues occur with oblique transmissions through glass surfaces with multi-layer coatings. As an example, Figure 11 shows the variation of the $I \rightarrow Q, U, V$ instrumental polarization as a function of time for the Swedish Vacuum Solar Telescope. Note the large discrepancy between the observed polarization and the theoretical model (Fig. 11a). Only by introducing purely empirical offsets can the theoretical model be fitted reasonably well. This

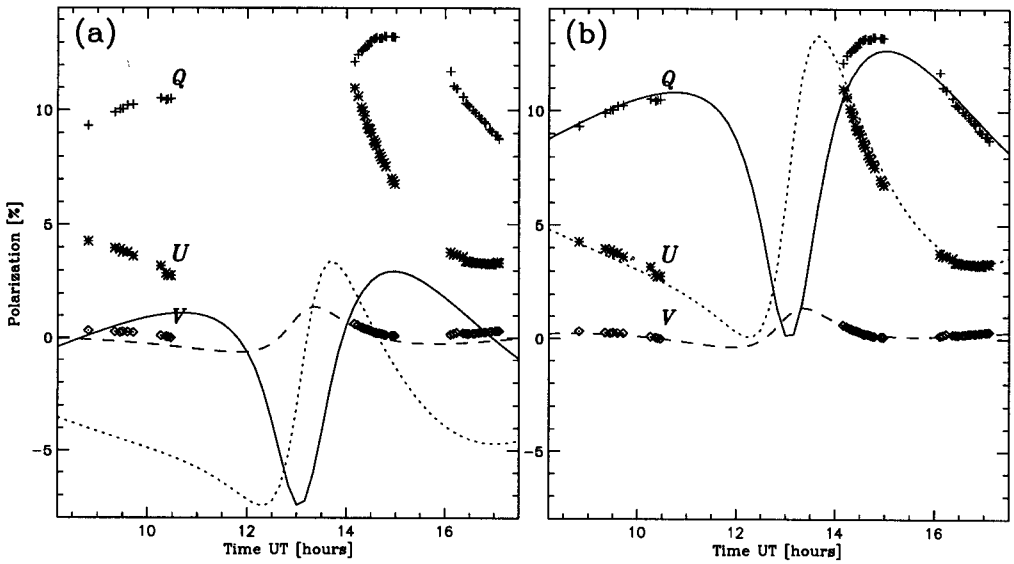

FIGURE 11. Instrumental polarization of the Swedish Vacuum Solar Telescope as a function of time for one particular day at 525 nm (markers). a) Lines show a best-fit theoretical model of the telescope polarization. b) Lines show the same theoretical model plus appropriate offsets to fit the data. (Courtesy Pietro Bernasconi)

illustrates the difficulty of modeling the instrumental effects of telescopes. This why the instrumental polarization and cross-talk are often measured directly and not modeled in a self-consistent way using tabulated optical constants for the involved materials.

The polarization of a stack of thin films on a substrate can be calculated using a matrix theory that is used in thin-film design (e.g. Macleod 1969). For the following, the index of refraction is generally a complex quantity of the form

$$n = \tilde{n} - ik \,, \tag{4.43}$$

where $\tilde{n}$ is the (real) index of refraction and k is the extinction coefficient. $k = 0$ for dielectrica. Both values are tabulated for common optical materials as a function of wavelength.

The layers are numbered from 1 to L with the first layer being closest to the substrate. Each layer has an associated index of refraction n_j and a geometrical thickness d_j. The substrate and the exterior medium have refractive indices n_s and n_m, respectively.

The complex reflection and transmission coefficients for an angle of incidence of θ_0 are given by

$$r = \frac{\eta_m E_m - H_m}{\eta_m E_m + H_m} \tag{4.44}$$

and

$$t = \frac{2\eta_m}{\eta_m E_m + H_m} \,, \tag{4.45}$$

where

$$\begin{pmatrix} E_m \\ H_m \end{pmatrix} = \mathsf{M} \begin{pmatrix} 1 \\ \eta_s \end{pmatrix} \,. \tag{4.46}$$

The matrix M is the product of all the matrices that describe the various layers, i.e.

$$\mathsf{M} = \mathsf{M}_L \mathsf{M}_{L-1} ... \mathsf{M}_2 \mathsf{M}_1 \,. \tag{4.47}$$

The 2 by 2 complex matrices M_j are given by

$$\mathsf{M}_j = \begin{pmatrix} \cos\delta_j & \frac{i}{\eta_j}\sin\delta_j \\ i\eta_j \sin\delta_j & \cos\delta_j \end{pmatrix} , \tag{4.48}$$

where

$$\delta_j = \frac{2\pi}{\lambda} n_j d_j \cos\theta_j . \tag{4.49}$$

θ_j can be calculated from Snell's law,

$$n_m \sin\theta_0 = n_j \sin\theta_j . \tag{4.50}$$

For s polarization, η is defined as

$$\eta = n\cos\theta , \tag{4.51}$$

and for p polarization, it is defined as

$$\eta = \frac{n}{\cos\theta} . \tag{4.52}$$

The Mueller matrix for transmission is then given by

$$\frac{1}{2}\begin{pmatrix} (T_s+T_p) & (T_s-T_p) & 0 & 0 \\ (T_s-T_p) & (T_s+T_p) & 0 & 0 \\ 0 & 0 & 2\sqrt{T_pT_s}\cos(\epsilon_p-\epsilon_s) & 2\sqrt{T_pT_s}\sin(\epsilon_p-\epsilon_s) \\ 0 & 0 & -2\sqrt{T_pT_s}\sin(\epsilon_p-\epsilon_s) & 2\sqrt{T_pT_s}\cos(\epsilon_p-\epsilon_s) \end{pmatrix} , \tag{4.53}$$

where

$$T_{s,p} = \frac{\eta_s}{\eta_m}|t_{s,p}|^2 \tag{4.54}$$

and

$$\epsilon_{s,p} = arg(t_{s,p}) . \tag{4.55}$$

To obtain the Mueller matrix for the reflected beam, $T_{s,p}$ is replaced by

$$R_{s,p} = |r_{s,p}|^2 , \tag{4.56}$$

and $\epsilon_{s,p}$ is given by

$$\epsilon_{s,p} = arg(r_{s,p}) . \tag{4.57}$$

Furthermore, the signs of the Mueller matrix elements in the lower right have to be changed to conform with the conventions for a reflected beam. The Mueller matrix for the reflected beam then becomes

$$\frac{1}{2}\begin{pmatrix} (R_s+R_p) & (R_s-R_p) & 0 & 0 \\ (R_s-R_p) & (R_s+R_p) & 0 & 0 \\ 0 & 0 & -2\sqrt{R_pR_s}\cos(\epsilon_p-\epsilon_s) & -2\sqrt{R_pR_s}\sin(\epsilon_p-\epsilon_s) \\ 0 & 0 & 2\sqrt{R_pR_s}\sin(\epsilon_p-\epsilon_s) & -2\sqrt{R_pR_s}\cos(\epsilon_p-\epsilon_s) \end{pmatrix} . \tag{4.58}$$

As an example, let us consider a mirror with $n = 1.2$, $k = 7.5$ (typical for aluminum at 630 nm). A beam incident at 45° will have a normalized reflection Mueller matrix of

$$\begin{pmatrix} 1.000 & 0.028 & 0.000 & 0.000 \\ 0.028 & 1.000 & 0.000 & 0.000 \\ 0.000 & 0.000 & -0.983 & -0.180 \\ 0.000 & 0.000 & 0.180 & -0.983 \end{pmatrix} . \tag{4.59}$$

However, if we add a 126-nm thick dielectric layer with an index of refraction of 1.4

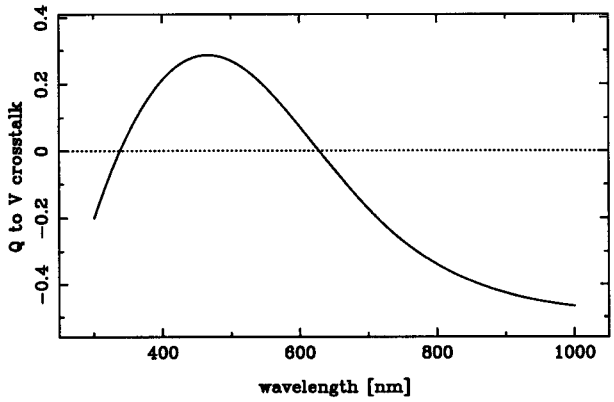

FIGURE 12. Variation of the $V \rightarrow Q$ cross-talk as a function of wavelength for an aluminum mirror overcoated with a 126-nm thick dielectrica with an index of refraction of 1.4 and an angle of incidence of 45°.

on top of the aluminum, we obtain

$$\begin{pmatrix} 1.000 & -0.009 & 0.000 & 0.000 \\ -0.009 & 1.000 & 0.000 & 0.000 \\ 0.000 & 0.000 & -1.000 & 0.000 \\ 0.000 & 0.000 & 0.000 & -1.000 \end{pmatrix} . \tag{4.60}$$

The cross-talk between Q and V has disappeared. Indeed, mirrors can be constructed that minimize the cross-talk using dielectric thin-film stacks. Nevertheless, while the I to and from Q terms are substantially reduced, they have not been eliminated completely. Furthermore, if we look at the wavelength-dependence of the V to Q cross-talk (see Fig. 12) even when assuming that the optical constants n and k are constant with wavelength, we see that there is a large variation with wavelength and that even the sign of the cross-talk changes. This is due to interference effects in the dielectric layer.

A dielectric layer of the same type with a thickness of only 65 nm leads to the following Mueller matrix

$$\begin{pmatrix} 1.000 & 0.014 & 0.000 & 0.000 \\ 0.014 & 1.000 & 0.000 & 0.000 \\ 0.000 & 0.000 & -0.858 & -0.514 \\ 0.000 & 0.000 & 0.514 & -0.858 \end{pmatrix} , \tag{4.61}$$

which maximizes the crosstalk between Q and V. Indeed, it has been noticed that a thin oil film on an aluminum mirror can lead to a big change in the telescope Mueller matrix and that it varies strongly with wavelength. In general, aluminum is covered with a thin layer of aluminum oxide that changes the Mueller matrix with respect to a clean aluminum layer (Sankarasubramanian et al. 1999).

If no thin-film layers are used, the matrix theory approach reduces to the usual Mueller matrices for reflection and transmission on/through dielectric and metallic surfaces, which, for an air-dielectric interface, are given by

$$\mathsf{M}_r = \frac{1}{2}\left(\frac{\tan\alpha_-}{\sin\alpha_+}\right)^2 \begin{pmatrix} c_-^2 + c_+^2 & c_-^2 - c_+^2 & 0 & 0 \\ c_-^2 - c_+^2 & c_-^2 + c_+^2 & 0 & 0 \\ 0 & 0 & -2c_+c_- & 0 \\ 0 & 0 & 0 & -2c_+c_- \end{pmatrix} \tag{4.62}$$

and

$$\mathsf{M}_t = \frac{1}{2}\frac{\sin 2i \sin 2r}{(\sin\alpha_+ \cos\alpha_-)^2}\begin{pmatrix} c_-^2+1 & c_-^2-1 & 0 & 0 \\ c_-^2-1 & c_-^2+1 & 0 & 0 \\ 0 & 0 & 2c_- & 0 \\ 0 & 0 & 0 & 2c_- \end{pmatrix}, \tag{4.63}$$

where

$$\alpha_\pm = i \pm r\,, \tag{4.64}$$

$$c_\pm = \cos\alpha_\pm\,, \tag{4.65}$$

and i and r are the angle of the incident light and the refracted light, which are related by Snell's law according to

$$\sin i = n \sin r\,, \tag{4.66}$$

where n is the index of refraction of the dielectric.

For reflections off metal surfaces, the Mueller matrix for the reflected beam is given by

$$\mathsf{M}_r = \frac{1}{2}\begin{pmatrix} \rho_s^2+\rho_p^2 & \rho_s^2-\rho_p^2 & 0 & 0 \\ \rho_s^2-\rho_p^2 & \rho_s^2+\rho_p^2 & 0 & 0 \\ 0 & 0 & 2\rho_s\rho_p\cos\delta & 2\rho_s\rho_p\sin\delta \\ 0 & 0 & -2\rho_s\rho_p\sin\delta & 2\rho_s\rho_p\cos\delta \end{pmatrix}, \tag{4.67}$$

where the real quantities ρ_s, ρ_p, and $\delta = \phi_s - \phi_p$ are defined by

$$\rho_s e^{i\phi_s} = -\frac{\sin(i-r)}{\sin(i+r)} = \frac{\cos i - n\cos r}{\cos i + n\cos r} \tag{4.68}$$

and

$$\rho_p e^{i\phi_p} = \frac{\tan(i-r)}{\tan(i+r)} = \left(\frac{n\cos r - \cos i}{\cos i + n\cos r}\right)\left(\frac{n\cos r\cos i - \sin^2 i}{n\cos r\cos i + \sin^2 i}\right) \tag{4.69}$$

and i and r are the angles of the incident light and the (complex) angle of the refracted light, which are related by Snell's law according to

$$\sin i = n \sin r\,, \tag{4.70}$$

where n is the complex index of refraction of the metal. To evaluate the equations above, it is useful to realize that

$$n\cos r = \sqrt{n^2 - \sin^2 i}\,. \tag{4.71}$$

4.2.3. *Polarized scattered light*

When observing the polarization of a faint source close to a very bright source, scattered, instrumentally polarized light from the bright source can influence the polarimetry of the faint source. The following example and discussion is taken from Keller and Sheeley (1999), who observed the polarization of the solar chromosphere just above the limb of the solar disk using the McMath-Pierce solar telescope.

Figure 13 shows how the apparent polarization of the OI 777 nm triplet varies with geocentric position around the solar limb. Clearly, the effect reverses sign at a position angle near 135° from the geographic north direction. However, the reversal does not occur at the same position angle for all three lines, as if the instrumental effect were being supplemented by different scattering polarizations from each line. Other data sets also showed OI 777.5 nm reversals close to the 45° and 135° locations.

The magnitude of this instrumental effect is on the order of 10^{-3} to 10^{-2}, i.e. it is comparable to any true solar scattering polarization signal. Regular instrumental polarization cannot be the explanation since the Q/I signal due to instrumental polarization

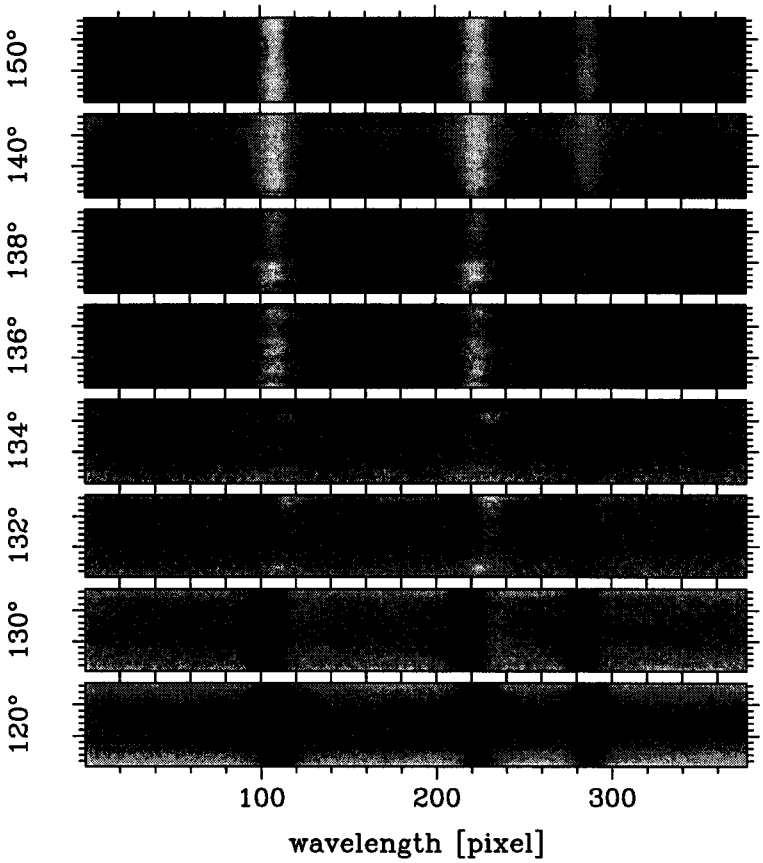

FIGURE 13. Observed Stokes Q/I signal in the OI 777 nm triplet about 1″ above the limb as a function of position angle, measured clockwise from geographic north. Lighter-than-average shading denotes polarization along the limb and darker-than-average shading denotes polarization perpendicular to the limb.

has no spectral signature. Empirically, the effect seems to be most pronounced for lines that are in absorption near disk center, but which weaken toward the limb and then go into emission above the limb. Also, telluric lines do not show this effect at all.

When observing above the solar limb, there is a contribution to the signal due to scattered light from the solar disk. While light from the solar limb due to seeing and telescope motion will have the same telescope Mueller matrix as compared to the chromospheric light, there will also be scattered light from all over the solar disk. Since the latter is not following the same path in the optical system as the true chromospheric spectrum (see Fig. 14), it exhibits a different instrumental polarization. Furthermore, the Mueller matrix describing the scattering process is not necessarily equivalent to the regular Mueller matrix for oblique reflection on a metallic coating with a different angle of incidence (e.g. Harvey & Vernold, 1997). In general, the Mueller matrix for scattering has to be calculated by performing a Fourier decomposition of the mirror surface profile that includes the dust on the mirror. The diffraction from each sinusoidal grating (corresponding to one Fourier component) has to be determined. The coherent sum of all these diffracted rays has to be considered when calculating the Mueller matrix for the scattering process.

In the following we construct a model of the influence of polarized, instrumentally

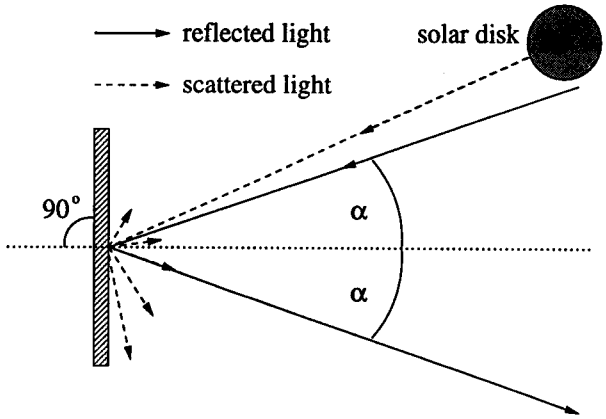

FIGURE 14. Light paths for obliquely reflected (from above the solar limb) and scattered light (from all over the solar disk) on a flat mirror. Note that scattered light does not follow the rule of equal angles of incidence for the incoming and outgoing beams. Part of the scattered light goes in the same direction as the reflected light, thus contributing to the measured signal.

scattered light on precision linear polarization measurements above the limb. For simplicity we will assume that there is only instrumental cross-talk between I and Q, i.e. we assume that there are no U and V signals. The instrumental cross-talk can then be described by

$$\begin{pmatrix} i \\ q \end{pmatrix} = \begin{pmatrix} M_{11} & M_{12} \\ M_{21} & M_{22} \end{pmatrix} \begin{pmatrix} I \\ Q \end{pmatrix} , \tag{4.72}$$

where lower case letters indicate the measured quantities and upper case letters indicate the true solar signal. With the Mueller matrices M^r and M^s describing the reflected and scattered light, respectively, the observed Stokes q/i signal is given by

$$\frac{q}{i} = \frac{M^r_{21} I_r + M^s_{21} I_s + M^r_{22} Q_r + M^s_{22} Q_s}{M^r_{11} I_r + M^s_{11} I_s + M^r_{12} Q_r + M^s_{12} Q_s} , \tag{4.73}$$

where I_r, Q_r, I_s, and Q_s are the solar Stokes I and Q signals for the reflected and the scattered beams, respectively.

This equation can be simplified by realizing that the terms $M^r_{12} Q_r$ and $M^s_{12} Q_s$ in the denominator are about three orders of magnitude smaller than the other terms in the denominator. $M^{r,s}_{12}$ as well as $Q^{r,s}$ are all on the order of a few percent or less as compared to $M^{r,s}_{11}$ and $I^{r,s}$, which are of order unity. Furthermore, since the instrumentally scattered light comes from all over the solar disk, we would not expect any net contribution to the true polarization signal, i.e. $Q_s = 0$ is a good assumption. Finally, $M^{r,s}_{11} = M^r_{22} = 1$ is a reasonable assumption that has no significant influence on our analysis. We thus obtain

$$\frac{q}{i} = M^r_{21} + \Delta M \frac{I_s}{I_r + I_s} + \frac{Q_r}{I_r + I_s} , \tag{4.74}$$

where $\Delta M = M^s_{21} - M^r_{21}$. M^r_{21} is the linear polarization induced by the telescope mirrors and simply adds an offset. ΔM does not change with time as the heliostat rotates because the scattered and reflected light share the same optical path after leaving the heliostat. Finally, I_s is expected to show a spectral dependence similar to the integrated photospheric flux spectrum and should be independent of the exact height above the solar limb because it is due to large-angle (on the order of 0.25 degrees) scattering that should not vary rapidly over small angles of the order of 1″.

Although the $Q_r/(I_r + I_s)$ term may cause slight variations in q/i, the main influence of instrumentally scattered polarized light is contained in the term $\Delta M I_s/(I_r + I_s)$. For

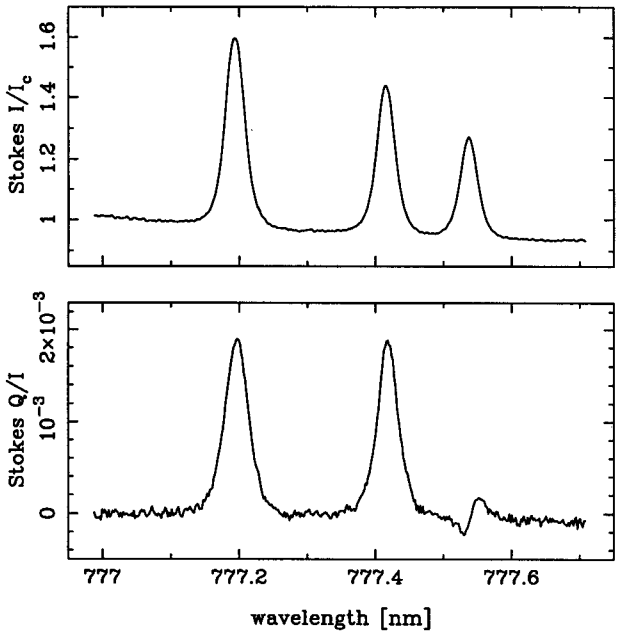

FIGURE 15. True scattering polarization in the OI triplet at 777 nm about 1″ above the limb. The polarization of the continuum has been set to zero because the observations do not allow a correct measurement of the continuum polarization.

telluric lines, this term is independent of wavelength because they have the same shape for reflected and scattered light, which explains why they do not show the effect. Also, the spectral variation of this term is largest for lines that show a large difference between the photospheric and the chromospheric spectra, which explains why the effect is largest for strong emission lines that are in absorption on the disk.

The dependence of ΔM on position angle β of the polarimeter with respect to the geographic north direction can easily be understood. The combined Mueller matrices for all telescope elements for reflected and scattered light have all reflections in common after the heliostat mirror. Under the assumption of weakly polarizing elements, the multiplication of the Mueller matrices can be approximated by the sum of the Mueller matrices (see Stenflo 1994). The difference between the two Mueller matrices for the whole telescope is therefore almost equivalent to the difference between the Mueller matrices for reflection and scattering at the heliostat alone. These two matrices depend on the sun's declination (which can be assumed to be constant during a day) and on the angle, β, of the positive Stokes Q direction with respect to the geographic north direction. The latter corresponds to a simple rotation of the Stokes coordinate system, hence ΔM is proportional to $\cos 2\beta$.

The simple dependence of ΔM on position angle can be used to determine the true solar signal. If q/i is measured at two or more position angles, we can remove the β-dependence by performing a linear regression with respect to $\cos 2\beta$, and obtain the polarization $Q^r(\lambda)/(I^r(\lambda) + I^s(\lambda))$ up to a constant that corresponds to the continuum polarization. Figure 15 shows this quantity for the OI triplet, and, as expected, indicates much less scattering for the 777.5 nm line than for the other two lines. A similar regression can be made if observations are taken at various distances from the limb.

To avoid problems with instrumentally polarized scattered light, the foremost requirements is to keep the mirrors clean. Careful washing can reduce scattered light drastically.

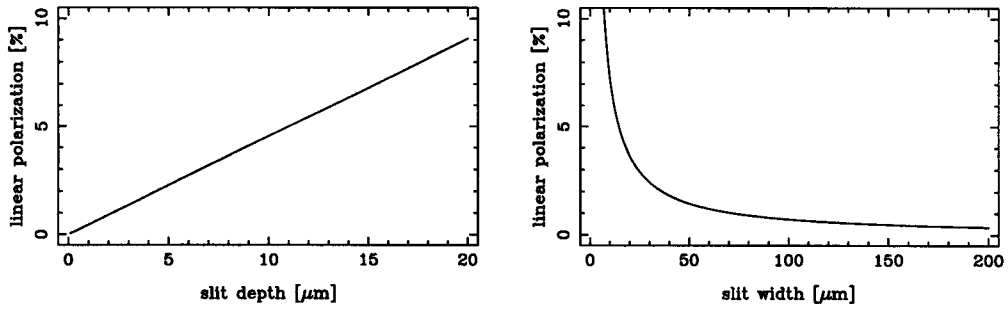

FIGURE 16. Variation of linear polarization induced by a narrow and thin steal slit as a function of slit depth (for a width of 16μm) and width (for a depth of 10μm) at 632.8 nm according to the theory of Slater (1942).

4.2.4. *Polarization due a narrow spectrograph entrance slit*

While the spectrograph entrance slit is really part of an instrument and not the telescope, it is adequate to discuss this effect here. When the width of a slit is comparable to the wavelength of the incident light, the slit acts as a partial polarizer. Indeed, entrance slits of modern spectrographs are often on the order of 10 to 20 times the wavelength, where such effects may become important. Slit polarization was first observed by Fizeau in 1861 and later by Zeeman in 1912 when he measured the polarization of spectral lines. It is obvious that a slit polarizes in the same way that a wire-grid polarizer works. Therefore one might expect that the slit polarization would be much reduced when using dielectric media for the slit. However, various reports in the literature seem to indicate that it does not matter much whether the slit is made of a conducting or a dielectric material (to within a factor of 2). Various models have been developed to calculate this polarization as a function of width, depth, and material properties of the slit.

An overview of various theories has been given by Ismail (1985). The theory by Slater (1942) based on microwave wave-guide theory seems to compare best with actual measurements. It also generally leads to larger values of the polarization than other theories, therefore providing a reliable upper limit to the expected slit polarization.

The expected fractional polarization from Slater's (1942) theory is given by

$$P = \frac{e^{-2a_p z} - e^{-2a_s z}}{e^{-2a_p z} + e^{-2a_s z}} \tag{4.75}$$

where

$$a_s = \frac{2}{b}\sqrt{\frac{\omega\epsilon_0}{2\sigma}}\left[1 - \left(\frac{n\lambda}{2b}\right)^2\right]^{-\frac{1}{2}} \tag{4.76}$$

and

$$a_p = a_s\left(\frac{n\lambda}{2b}\right)^2 . \tag{4.77}$$

b is the slit width, z is the slit depth, ϵ_0 is the permittivity of free space, ω is the angular frequency of the light and λ is the wavelength of light, σ is the conductivity of the slit material, and n is the wave order. Since $n = 1$ gives the largest amount of polarization, it is sufficient to assume $n = 1$ to estimate an upper limit for the slit polarization. Figure 16 shows theoretical calculations of the induced linear polarization for a steel slit as a function of slit depth and width, which is in reasonable agreement with observations.

These calculations indicate that a narrow slit should be made as thin as possible, at least at the edges to reduce the amount of polarization introduced by the narrow slit.

Very thin slits can be manufactured by evaporating a metal film on a glass substrate or by laser-cutting a very thin metal foil.

4.2.5. *Mitigating instrumental polarization and cross-talk*

There are various approaches to mitigate instrumental polarization and cross-talk. Among the more common approaches are:

- avoiding oblique reflections;
- compensating instrumental polarization and cross-talk with:
  - retarders,
  - partial polarizers such as tilted glass plates,
  - crossing mirrors at 90° (see above),
  - use two or four mirror arrangements to compensate for a single oblique reflection off a mirror;
- measure and take into account in data reduction.

4.3. *Angle-dependence of polarizers and retarders*

4.3.1. *Angle-dependence of polarizers*

While sheet polarizers and similarly constructed polarizers are basically insensitive to the angle of incidence, crystal polarizers have a limited angle of incidence under which they work. For calcite-based polarizers, this is on the order of 10°, which is due to the critical angles for total internal reflection at the inner surfaces being different for ordinary and extraordinary rays. The transmitted light is polarized when the incidence angle is below this limit. Otherwise rays are either both reflected or transmitted, depending on the construction of the polarizer.

Beams through crystals behave optically differently from glass because the index of refraction depends on the angle of the ray with respect to the crystal optic axis. The most common crystal aberrations are defocus and astigmatism. Recent versions of some optical ray-tracing software (e.g. ZEMAX) can perform the basic crystal calculations.

As an example, we consider a calcite beam splitter. Obviously, ordinary and extraordinary rays travel different distances (see Fig. 5). Therefore, there will be a focus difference between the two beams. To avoid this problem, the calcite block can be split into two pieces, which are crossed at 90°. This is called a *Savart plate*, which has a splitting that is reduced by factor of $\sqrt{2}$, but the defocus has disappeared. However, the two beams will show astigmatism in opposite directions, which is due to the crystal aberrations, something that is not observed in isotropic materials.

Another approach consist in using the two calcite blocks in the same orientation, but add a half-wave plate between them to exchange the ordinary and extraordinary beams, which is called a *modified* Savart plate. The crystal astigmatism is now the same in the two beams. By adding a cylindrical lens, the astigmatism can be compensated for. As a rule of thumb for calcite, the astigmatic focus difference amounts to about 5% of the calcite thickness.

4.3.2. *Angle-dependence of retarders*

Retarders can have strong variations of retardation with angle of incidence. For a rotation around an axis that is parallel to the optic axis, the angle between the beam and the optic axis of the crystal does not change. Therefore, both e and o beams will travel at the same speed, but through more material. For small angles of incidence θ, Snell's law tells us that the angle of the beam within the retarder has an angle of θ/n, where n is the geometrical mean of the two indices of refraction, i.e. $n = \sqrt{n_e n_o}$. The

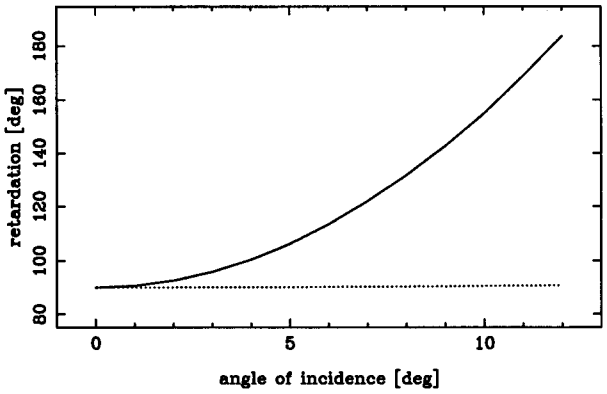

FIGURE 17. Variation of retardance with angle of incidence for 2-mm thick compound zero-order (solid line) and true zero-order (dotted line) quartz quarter-wave plates at 632.8 nm.

increase of the path length due to the inclined beam is therefore given by $d/\cos(\theta/n)$ such that the relative path difference becomes

$$(N\lambda)(\theta) = \frac{d}{\cos\theta/n}(n_e - n_o) \ . \tag{4.78}$$

With θ measured in radians and using the approximation $\cos x \approx 1 - x^2/2$, and using the expression for $N\lambda$ at normal incidence, we obtain the (approximate) angular variation of the retardation as

$$\delta(N\lambda)(\theta) = +\frac{N\theta^2}{2n^2} \ . \tag{4.79}$$

For a 2-mm thick compound zero-order quartz quarter-wave plate, a rotation of 10° will make it almost into a half-wave plate (see Fig. 17), while a true zero-order retarder shows barely any change in retardation.

For a rotation perpendicular to the optic axis, one derives the same equation, but with the opposite sign. For larger angles the theory needs be corrected in the sense that the e and o beams in the retarder have different angles and therefore also exit the beam at two slightly different locations.

It is evident that the angle-dependent variation is linear in N and quadratic in the angle θ. Also, a compound zero-order retarder made from to thick retarders of the same material has the same angle dependence as a single multi-order retarder of the same thickness because one plate is rotated around an axis parallel to the optic axis and the other plate around an axis perpendicular to the optic axis. While some catalogs and even text books claim that compound zero-order and true-zero order waveplates show the same angle dependence, this is not correct. If one has a fast beam, it is important to use true zero-order retarders.

Kerr cells, liquid crystals, and PEMs all behave like true zero-order retarders. However, for PEMs, the retardance decreases with increasing distance from the center. Hence, it is possible to place a PEM into an optical beam in such a way that the angular and spatial variation compensate each other to a large degree. It is therefore possible to use PEMs with very fast beams.

Pockels cells have only a few degrees acceptance angle because of strong crystal effects.

4.4. *Temperature dependence of retarders*

Retarders can be particularly temperature sensitive, in particular multiple order waveplates. The optical path difference variation between ordinary and extraordinary rays, to first order, is given by

$$\delta d\,(n_e - n_o) + d\,(\delta n_e - \delta n_o)\ , \tag{4.80}$$

where δ indicates variations with temperature. Using the coefficient of thermal expansion $\alpha = \delta d/d$, we obtain

$$\delta N = N\left(\alpha + \frac{\delta n_e - \delta n_o}{n_e - n_o}\right) \tag{4.81}$$

For quartz, the quantity in parentheses amount to -1.0×10^{-4} per degree Kelvin at a wavelength of 632.8 nm. For a 2 mm thick multi-order quarter-wave retarder, this translates into a retardation variation of about 1 degree per degree Kelvin. Compound zero-order waveplates have the same temperature dependence as true zero-order retarders because the two plates compensate each other to a large degree. Achromatic zero-order retarders made from different materials can have larger effects due to temperature changes because the two materials have different coefficients of thermal expansion and temperature variations of the index of refraction.

4.5. *Polarized interference fringes*

When the retardation of a variable retarder is varied, the optical path length within the retarder also changes. Multiple reflections between the surfaces of the retarder lead to spectral fringes, whose pattern changes when the retardation is changed (because of the change in optical path length). A polarized spectrum (difference between two measurements with different retardations) will show a fringe pattern (see Fig. 18). This effect has been described by Oakberg (1995) for photoelastic modulators. Similar fringe patterns have also been observed in liquid crystal retarders and fixed retarders. The latter is due to the fact that the expression for the retardance of a birefringent plate given above is only a first-order approximation. Multiple reflections at the surfaces must be taken into account to obtain the higher-order correction terms. When including the higher-order terms, fringes in the retardation occur (e.g. Clarke & Grainger 1971). These can be reduced by applying an appropriate anti-reflection coating to the birefringent material.

Tilting, wedging, and coating the retarders reduces the fringe amplitude considerably. However, at the 1×10^{-5} level, polarized fringes are almost always present. Often the fringes can be removed during the data reduction by an appropriate filtering in the Fourier domain.

4.6. *Detector-induced errors*

Any real detector system has non-linearities, which are mostly due to the analog readout electronics. When trying to look for very small polarization signals (e.g. 1×10^{-5} of the intensity) on top of a small instrumental polarization signal of 1%, non-linearities become important, as is shown in the following.

Let the measured signal S be a quadratic function of the incoming intensity I

$$S = aI^2 + bI + c\ , \tag{4.82}$$

which is the most simple form for a non-linear behavior. b represents the (arbitrary) gain, c any remaining influence of bias or dark current that has not been correctly removed, and a models the non-linearity. The constant term also models effects of stray-light in a filter or a spectrograph.

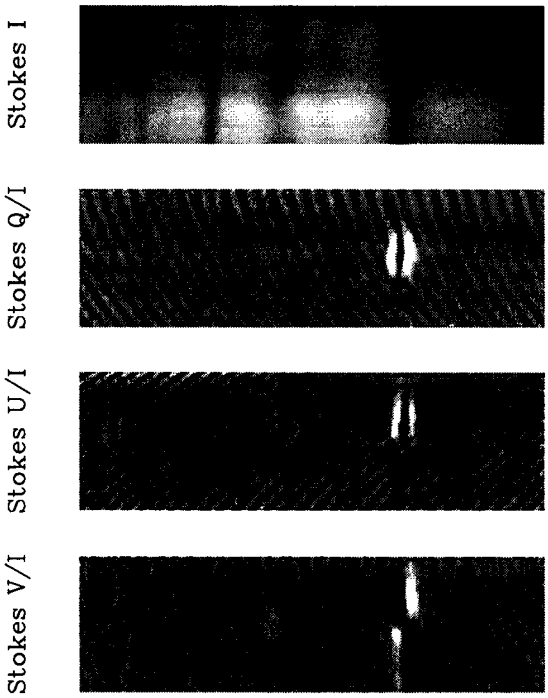

FIGURE 18. Polarized interference fringes in highly sensitive vector measurements of a sunspot spectrum around the HeI 1083.0 nm line observed with ZIMPOL I (see below).

For unpolarized incoming light, the two opposite polarization states measured by the polarimeter are

$$I^+ = I + \delta I \,, \quad I^- = I - \delta I \,, \tag{4.83}$$

where δI is the instrumental polarization signal.

The measured amount of polarization is determined from

$$P_m = \frac{S^+ - S^-}{S^+ + S^-} \,, \tag{4.84}$$

which in the ideal case of $a = 0$, $c = 0$ corresponds to the instrumentally introduced polarization

$$P = \frac{bI^+ - bI^-}{bI^+ + bI^-} = \delta \,. \tag{4.85}$$

In the case of non-linearities and an offset error, the apparent, measured polarization signal becomes

$$P_m = \frac{2a\delta I^2 + b\delta I}{aI^2 + a\delta^2 I^2 + bI + c} \,. \tag{4.86}$$

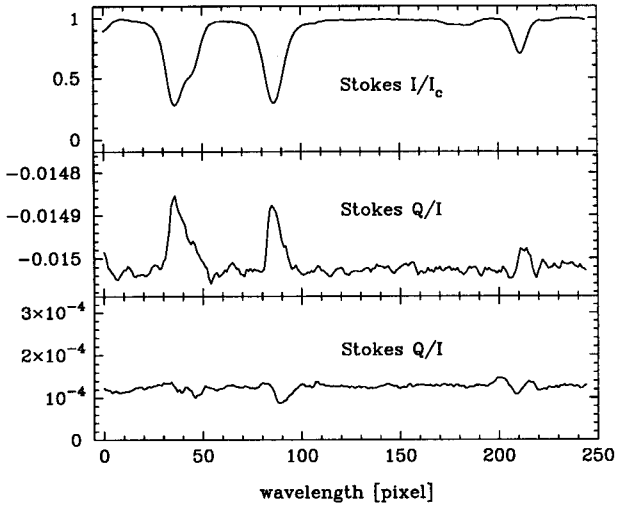

FIGURE 19. Artificial polarization signal created by the coupling of non-linearities in the CCD readout electronics and instrumental polarization for a solar spectrum observed at disk center. The top panel shows the Stokes I profile normalized with the continuum intensity I_c. The center panel shows Stokes Q/I in the case of -1.5% linear polarization induced by oblique reflections in the telescope. The lower panel shows the same linear polarization after compensating the linear polarization induced by the telescope. The remaining structure seen in the lower panel is only due to magnetic fields in the quiet sun.

As expected, in the absence of instrumental polarization, i.e. $\delta = 0$, no polarization would be measured.

In the following we will only keep terms up to second order in a, δ, and their cross-products. First, we assume that $c = 0$. The measured polarization then becomes

$$P_m = \delta \left(1 + \frac{a}{b} I\right) . \tag{4.87}$$

The observed polarization has therefore an additional component that is essentially proportional to aI, the coefficient of the non-linear term times the intensity. If the detected signal corresponds to a spectrum, the measured polarization is not constant anymore, but has a Stokes I-like additive component.

To measure very small polarization signals in the presence of non-linearities in the detector system, it is necessary to minimize the instrumental polarization. After normalizing Stokes I with the continuum intensity I_c, variations of Stokes I are of order unity. A typical value for the non-linear term is $a/b = 0.01$. To achieve a sensitivity of 1×10^{-5}, the instrumental polarization δ must be smaller than 1×10^{-3}. This is particularly hard to achieve for linear polarization where a typical value for existing solar telescopes is $\delta = 0.05$. Therefore, a typical magnitude of the coupling of instrumental polarization with non-linearities in the detector system is 5×10^{-4}.

Figure 19 compares two linear polarization measurements of the same spectral region with and without compensation of the instrumental polarization. The ZIMPOL I camera used for those measurements did show a non-linearity of about $a/b = 1.4\%$. The simple model developed above explains the sign as well as the magnitude of the effect.

The other case is $a = 0$. The measured polarization then becomes

$$P_m = \delta \left(1 - \frac{c}{bI}\right) . \tag{4.88}$$

Since I shows structure, e.g. spectral lines, the observed polarization will show signatures

proportional to $1/I$. Any offset such as bias, dark current, and stray-light must be removed to a high degree. However, due to minuscule changes in the observing conditions (e.g. variation of the bias with time), there is often an offset error of approximately 1×10^{-3}. Therefore, this effect is about one order of magnitude smaller than the influence of non-linearities under realistic circumstances. It disappears completely if there is no instrumental polarization.

5. Examples of astronomical spectropolarimeters

5.1. *Introduction*

A large variety of astronomical spectropolarimeters have been designed and built. It is outside of the scope of this chapter to give an overview of all the various approaches and instruments. Instead, I selected a few examples with which I have personal experience. Other polarimeters that are used for night-time applications have been discussed by Tinbergen (1996). Solar polarimeters that have produced significant scientific results but are not discussed any further here include the Advanced Stokes Polarimeter (Lites 1996) based on a rotating retarder and the Tenerife Infrared Polarimeter (Martínez Pillet et al. 1999), which is based on FLCs.

5.2. *Sensitive stellar polarimeter*

A sensitive method for stellar circular polarimetry was developed by Semel et al. (1993). It is based on a rotating quarter-wave plate and a double-calcite beam-splitter, which produce two beams corresponding to opposite circularly polarized light. The quarter-wave plate can be rotated to $+45°$ and $-45°$ with respect to the polarization axes of the beam-splitter. Both beams are recorded simultaneously. The quarter-wave plate is then rotated by 90° and another image is exposed. The four measurements of the same object are then combined to obtain an estimate of the Stokes V/I ratio that is largely free of effects from seeing and gain variations between different detector areas if the polarization signal is small. This approach has been used in stellar polarimetry with great success by Donati et al. (1990, 1999). It can be applied to any polarized Stokes parameter.

This approach also works very well for solar applications where the spectrum in the first and the second exposures are different. Consider the measured intensities in the two beams in the first exposure after subtraction of the dark current (for the case of Stokes V)

$$S_1^l = g_l \alpha_1 (I_1 + V_1), \quad S_1^r = g_r \alpha_1 (I_1 - V_1). \tag{5.89}$$

The subscript 1 indicates the first exposure, the subscripts l and r indicate the left and the right beams of the polarizing beam-splitter. S describes the measured signal, g the gain in a particular beam, and α the average transmission of the atmosphere and the instrument for a given exposure.

In the second exposure, after the retarder has been rotated, the measured signals are given by

$$S_2^l = g_l \alpha_2 (I_2 - V_2), \quad S_2^r = g_r \alpha_2 (I_2 + V_2). \tag{5.90}$$

Note that the incoming intensity in the second exposure may be completely different from the first exposure. Such changes may be due to seeing as well as instrumental changes. This also includes a shift of the two beams between exposures due to beam-wobble induced by rotation of a wave plate.

The following combination of these four measured intensities removes the effect of

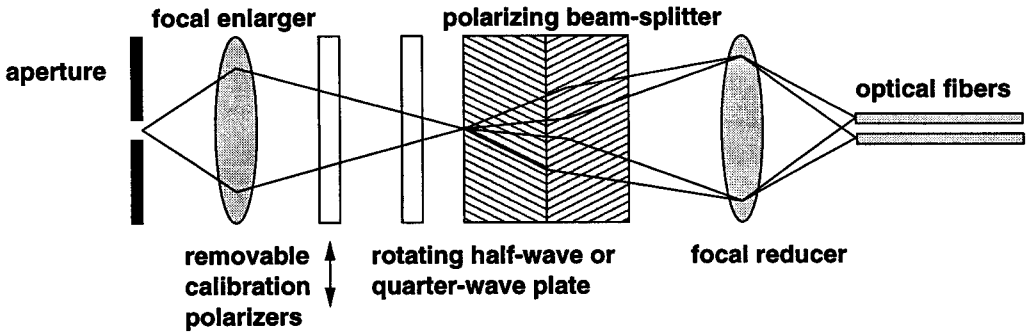

FIGURE 20. Optical layout of the MuSiCoS polarimeter by Donati et al. (1999). An entrance aperture provides a fixed field of view independent of seeing. A focal enlarger provides a slow beam through the polarimeter to avoid large angles of inclination on the polarization optics. Circular and linear polarizers can be inserted to calibrate the polarimeter. A rotating quarter-wave or half-wave plate provides the beam exchange. A polarizing beam-splitter splits the beam into two opposite polarization states that are reimaged onto the ends of two fibers that lead to the echelle spectrograph.

transmission changes and differential gain variations of different detector areas:

$$\frac{1}{4}\left(\frac{S_1^l}{S_2^l}\frac{S_2^r}{S_1^r}-1\right)=\frac{1}{2}\frac{I_2V_1+I_1V_2}{I_1I_2-I_2V_1-I_1V_2+V_1V_2}\,. \tag{5.91}$$

In the case of $V \ll I$, this is equivalent to

$$\frac{1}{2}\left(\frac{V_1}{I_1}+\frac{V_2}{I_2}\right). \tag{5.92}$$

Therefore we obtain the average V/I signal of the two exposures. No spurious polarization signals are introduced. If V is comparable to I, the method can be extended to higher orders (Bianda et al. 1998).

Figure 20 shows the layout and the operating principle behind the MuSiCoS spectrograph developed by Donati et al. (1999). Due to problems with polarized fringes in the superachromatic retarders, the instrument currently uses a crystalline achromatic quarter-wave plate for circular polarization measurements and a rotation of the whole instrument for the linear polarimetry. It is planned to upgrade the system with Fresnel rhombs that are very achromatic but do not show significant polarized fringes at the spectral resolution of the MuSiCoS spectrograph. By combining many spectral lines from the echelle spectra, it is possible to achieve sensitivities on the order of $1 \cdot 10^{-4}$ with high spectral resolution. Results from this polarimeter are shown in the chapter by Mathys.

5.3. *Zurich Imaging Stokes Polarimeters*

5.3.1. *Introduction*

Photoelastic modulators are the preferred variable retarders for polarization modulation above 1 kHz, but their high modulation frequencies of 20 to 50 kHz are incompatible with the read-out rate of standard array detectors. A new instrument concept developed by Povel et al. (1990) reconciled the incompatibility between the slow CCD image sensor and the fast photoelastic modulators by using the CCD directly as a demodulator.

Here we describe two instruments that are based on this approach. ZIMPOL (**Z**urich **I**maging **P**olarimeter) I has been used for almost 10 years now, while the second generation instrument, ZIMPOL II has just started delivering the first scientific results. A more detailed description of the overall concepts can be found in Povel (1995).

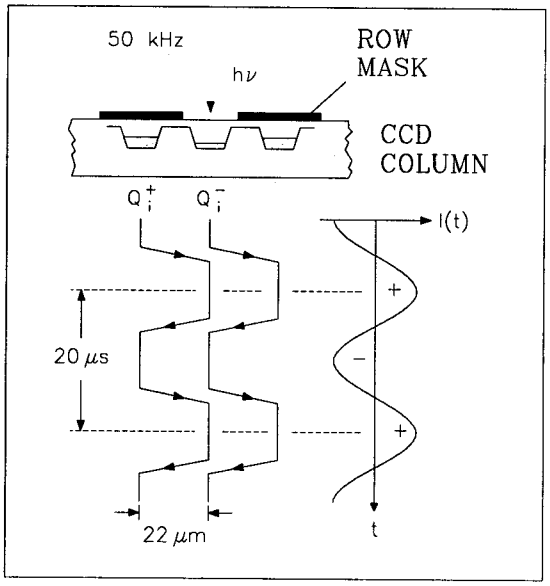

FIGURE 21. Principle of the ZIMPOL I CCD demodulator. A cross section through a part of the CCD sensor is shown at the top. The motion of the charge packets in the CCD are shown as a function of the modulation indicated in the right.

5.3.2. *CCD array as a fast demodulator*

The frame rate of regular CCD array detectors with a useful number of pixels is limited to about 1 kHz. For the detection of fast intensity modulations with frequencies of 50 to 100 kHz typical of PEMs, regular CCD array detectors cannot be used.

The charge shifting and storing capabilities of a CCD array detector, however, may be employed to operate the detector as a synchronous demodulator. The array is divided into photo-sensitive rows and storage rows that are shielded from light by a mask as shown in Fig. 21. The photo charges Q^+ generated in the photo-sensitive rows during the first modulation half-cycle are shifted into the storage row at the transition to the second modulation half-cycle. The photo charges Q^- generated during the second modulation half-cycle are shifted into the other storage row at the transition to the first modulation half-cycle. Q^+ and Q^- are simultaneously shifted from left to right and vice versa. While this procedure is repeated over many modulation cycles, Q^+ and Q^- are integrated alternately and synchronously to the modulation. Whenever the desired amount of charges have been accumulated, the charges are read out. From the digitized charge signals the normalized difference $P = (Q^+ - Q^-)/(Q^+ + Q^-)$ is calculated after correction for dark current and electronic offsets. P is proportional to the amplitude of the modulated signal. Note that pixel-to-pixel gain variations do not affect P. To avoid a reduction of the measured modulation amplitude by effects due to the finite transfer time of the charges from photo-sensitive to masked rows and vice versa, the transfer time must be about a factor of 100 faster than the modulation frequency. Furthermore, the charge transfer efficiency in both directions needs to be very high. Three-phase buried channel frame transfer CCD arrays designed for video applications meet these requirements.

A similar, yet much slower method was used by Stockman (1982) for differential imaging in astronomical applications.

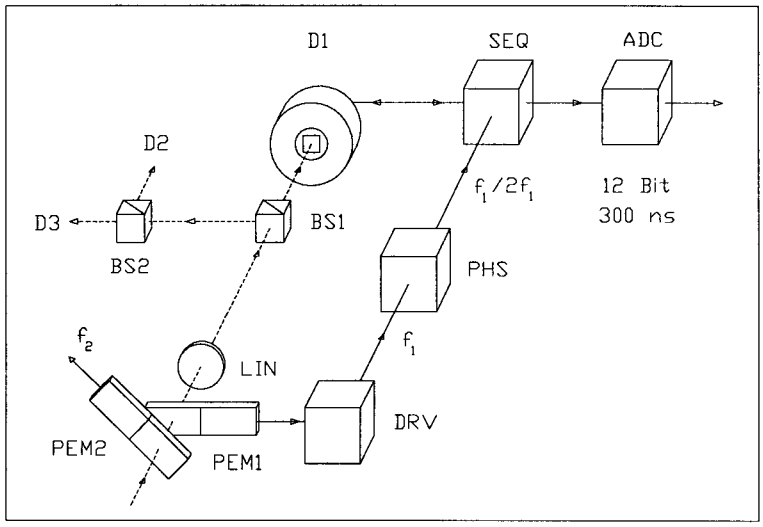

FIGURE 22. Setup for recording all four Stokes parameters with two photoelastic modulators. The orientation of the components is given with respect to Stokes Q. PEM1 (0°), PEM2 (45°): photoelastic modulators, LIN (22.5°): Glan linear polarizer, BS1, BS2: beam splitter cubes that direct the modulated light to detectors D1, D2, and D3.

5.3.3. *Polarimeter with PEM*

If a PEM is oriented under 45° with respect to Stokes Q and a linear polarizer follows at $-45°$ with respect to the PEM, the output intensity is given by

$$I'(t) = \frac{1}{2}\left(I + Q\cos\delta(t) + V\sin\delta(t)\right) , \tag{5.93}$$

where the retardation $\delta(t)$ has been given above. After the expansion in Bessel functions, Q is modulated at a frequency of $2\omega t$, while V is modulated at ωt. These two intensity modulations can be recovered separately by two different CCD cameras.

5.3.4. *ZIMPOL* I

The polarization modulator of ZIMPOL I consists of two photoelastic modulators and a linear polarizer (see Fig. 22). This configuration has been discussed in detail by Stenflo (1984, 1991). The combination of PEMs and the linear polarizer will henceforth been called modulator package. The modulators are commercially available devices that oscillate at a frequency of about 42 kHz.

A light beam with Stokes vector (I, Q, U, V) constant in time entering the modulator package produces intensity variations according to

$$I'(t) = \frac{1}{2}\left(I + Q\sqrt{2}J_2(A)\cos 2\omega_1 t + U\sqrt{2}J_2(A)\cos 2\omega_2 t + V\sqrt{2}J_1(A)\sin\omega_1 t\right) . \tag{5.94}$$

The oscillation frequencies of the two PEMs are given by ω_1 and ω_2, and J_1 and J_2 are the Bessel functions of order 1 and 2. The amplitude of both PEMs, A, is chosen such that $J_0(A) = 0$. For simultaneous measurements of all four Stokes parameters the light needs to be distributed to three separate detectors demodulating at frequencies ω_1, $2\omega_1$, and $2\omega_2$. This can be accomplished by two beam splitter cubes (see Fig. 22). More information on the design of ZIMPOL I can be found in Keller et al. (1992) and Povel et al. (1994).

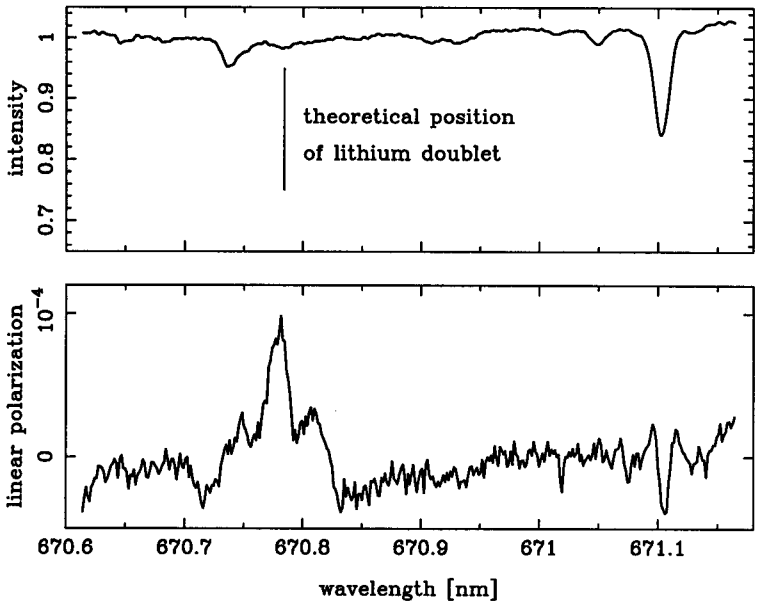

FIGURE 23. The lithium doublet at 670.9 nm is very difficult to measure in the solar intensity spectrum. The weak absorption line seen in intensity is due to CN. However, the lithium lines are resonance lines and therefore exhibit linear scattering polarization close to the solar limb. Since there are no other strongly polarizing lines close by, the lithium lines stand out in the polarization spectrum.

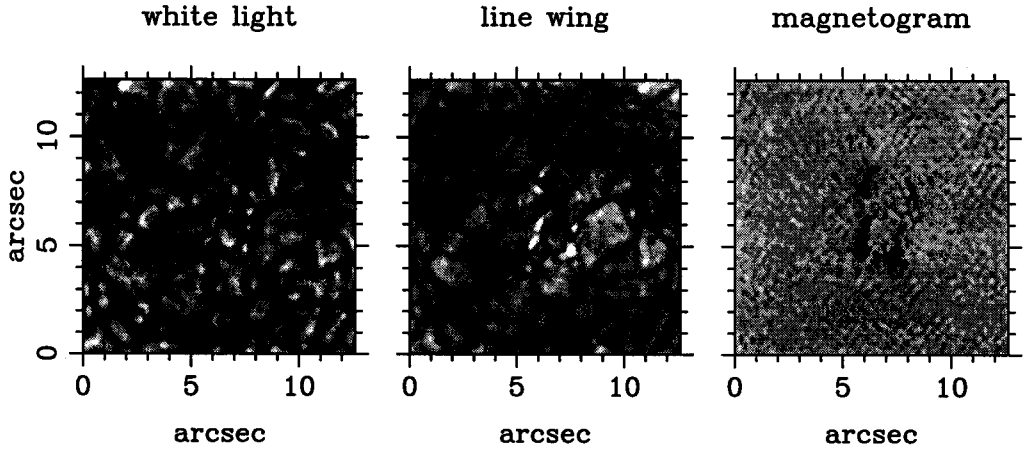

FIGURE 24. An example of a high-resolution observation of solar network magnetic fields close to disk center in CaI 610.3 nm using ZIMPOL I and speckle polarimetry to remove the effects of seeing. The magnetic fields are concentrated in very small areas and tend to be bright in both the white-light and the line-wing images.

5.3.5. *Scientific results from ZIMPOL* I

ZIMPOL I has provided a wealth of scientific results on solar polarization thanks to its high sensitivity that reaches down to a polarization of a few times 10^{-6}. Among many other things, it provided the first direct measurement of the field strength in solar intra-network fields (Keller et al. 1994) and opened the window to the *second solar spectrum* (see Stenflo in this volume). Figure 23 shows an example of the second solar spectrum. Thanks to its fast read-out rate and high modulation frequency, ZIMPOL I has been

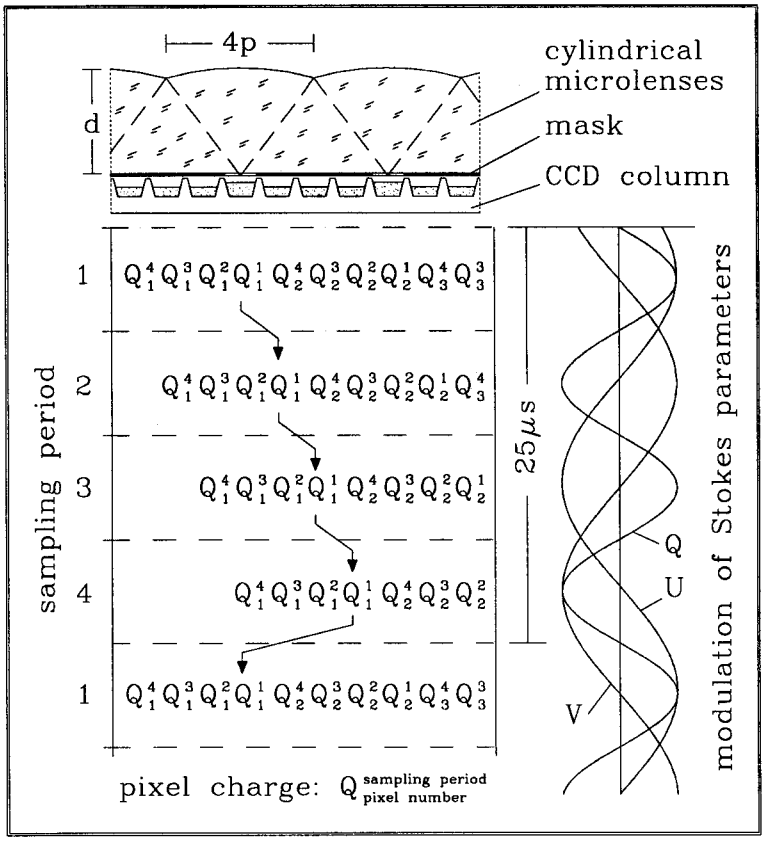

FIGURE 25. Principle of the ZIMPOL II demodulation scheme. The upper part shows a cross-section of the micro-lens array in a plane perpendicular to the pixel rows. p is the pixel size (22.5 μm). d is 1 mm. The right part shows the modulation of the Stokes parameters Q, U, and V. The left part shows the charge shifting scheme with respect to the modulation as envisioned in the conceptual design.

the premier instrument for image reconstruction techniques such as speckle imaging (see Fig. 24) and behind adaptive optics systems.

5.3.6. *ZIMPOL* II

A drawback of ZIMPOL I is its low efficiency due to the mask (a factor of 2) and the restriction of a single CCD demodulator to one frequency (a factor of 3). This efficiency loss of a factor of 6 is overcome by ZIMPOL II (see Stenflo et al. 1992), which was designed to use a cylindrical micro-lens array, two phase-coupled, synchronized PEMs with the same frequency, and an achromatic quarter-wave plate. Stokes V is modulated at $\sin(\omega t - \pi/4)$, Stokes Q at $\cos 2(\omega t - \pi/4)$, and Stokes U at $\sin(\omega t + \pi/4)$. Four sampling intervals in one modulation cycle are needed to record all four modulation states with a single, specially masked CCD (see Fig. 25). The light is focused on the CCD with a micro-lens array such that out of four pixels in one column only one is used for light detection while the remaining three are used for temporary charge storage. The four charge packets corresponding to four independent linear combinations of the four polarization states are sequentially shifted between the pixel rows in phase with the four-state modulation. After the CCD is read out, the four Stokes parameters can be calculated from the digitized pixel charges in the four interlaced images. In this

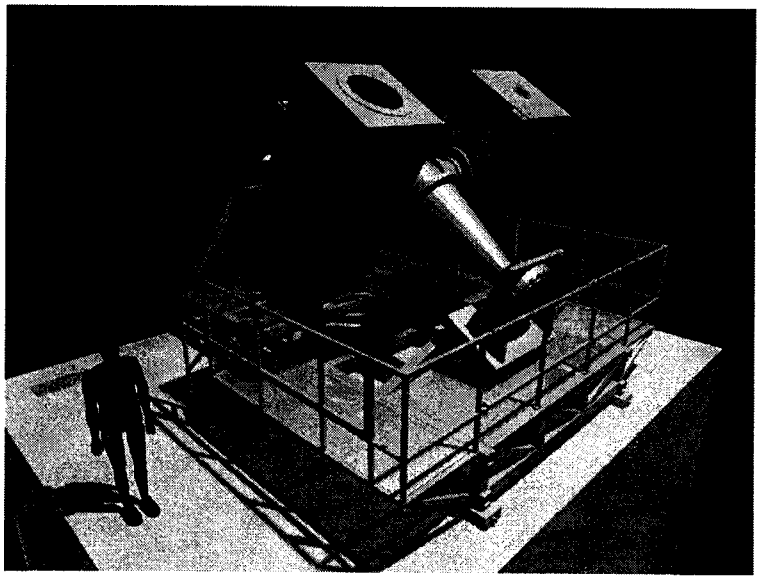

FIGURE 26. Artists impression of SOLIS on top of the Kitt Peak Vacuum Telescope building. The instrument with the large entrance window is the Vector-Spectromagnetograph.

way a precision imaging polarimeter recording simultaneously all four Stokes parameters may be realized with a single CCD sensor. In contrast, the three-CCD system used in ZIMPOL I requires accurate mechanical alignment and careful post-processing to combine the images from the three CCD cameras.

While possible, it proved hard to accurately align the micro-lenses on the CCDs (Gale et al. 1997). Furthermore, stray-light within the micro-lens-CCD assembly led to significant problems during the data reduction. Finally, the coupled PEMs have not been realized so far, which has prevented ZIMPOL II from measuring all four Stokes parameters simultaneously. However, using a modulator package based on FLCs will provide the required modulation waveforms (Gandorfer 1999). First scientific results from ZIMPOL II include an atlas of the second solar spectrum (Gandorfer 2000).

5.4. *SOLIS Vector-Spectromagnetograph*

5.4.1. *Introduction*

SOLIS, the Synoptic Optical Long-term Investigations of the Sun, will provide unique, modern observations of the Sun on a continuous basis for several decades. SOLIS consists of three instruments (a 50-cm vector spectromagnetograph, a 14-cm full-disk imager, and an 8-mm sun-as-a-star spectrometer) attached to a single equatorial mount. The mount is currently installed for testing at a preliminary site in Tucson. In its final configuration, SOLIS will be located on top of the Kitt Peak Vacuum Telescope (KPVT, see Fig. 26) and become operational by the end of 2001. More information can be found at `http://www.nso.noao.edu/solis`.

The SOLIS Vector Spectromagnetograph (VSM) operates in four different observing modes at three different wavelengths. The corresponding data products in the following list are given in parentheses.

(*a*) Photospheric full-disk vector-magnetograms using the FeI 630.15 and FeI 630.25 nm lines (field strength, azimuth, inclination, flux, Doppler velocity, continuum intensity);

Parameter	Specification
angular element	1.″0 by 1.″0
angular coverage	2048″ by 2048″
format	2048″ by 1″
geometric accuracy	<0.″5 rms after remapping
instrumental mtf	measurable to ±0.01
total mtf	<0.1 at frequencies greater than Nyquist
motion in RA	±0.25° for flat-fielding
scan rate	0.2-5.0 s/″
timing accuracy	better than 1 ms
spectral lines	FeI 630.1515, FeI 630.2507 nm, CaII 854.2089 nm, HeI 1083.0 nm
spectral resolution	200,000
wavelength ranges	630.1015-630.3007 nm, 854.2±0.1 nm, 1083.0±0.5 nm
polarimetry	630.2 nm: I,Q,U,V; 854.2 nm: I,V; 1083.0 nm: I
sensitivity	0.0002 per pixel in 0.5 s
relative accuracy	0.001
image stabilization	>40 Hz to improve spatial resolution
seeing monitoring	for information only
cloud detection	at user-specified level
cloud interruptions	for user-determined period

TABLE 6. Technical specifications for the SOLIS Vector-Spectromagnetograph (VSM)

(*b*) Chromospheric full-disk magnetograms using the CaII 854.2 nm line (line-of-sight magnetic flux, Doppler velocity, line core intensity);

(*c*) Full-disk HeI 1083.0 nm line characteristics (equivalent width, continuum intensity, Doppler velocity, line depth, line asymmetry, Doppler width, Si line width, Si line depth, Si Doppler velocity);

(*d*) Photospheric full-disk longitudinal magnetograms using the FeI 630.15 and 630.25 nm lines (line-of-sight magnetic flux).

Data products (a), (b), and (c) will be produced three times a day, while data product (d) will be produced once a day. Users may observe the same or subsets of these products such as vector-magnetograms of active regions at high temporal cadence or HeI 1083.0 nm equivalent width measurements of selected areas.

The CaII 854.2 nm and the HeI 1083.0 nm lines were chosen to provide a continuing record of the current data set from the KPVT. To measure vector magnetic fields outside sunspots in the visible part of the spectrum, it is indispensable to observe at least two spectral lines with different Landé factors. The FeI 630.15 and 630.25 nm lines were chosen because they are very suitable to measure vector magnetic fields in quiet as well as active regions of the photosphere. The Advanced Stokes Polarimeter (ASP), an instrument that delivers precise vector field measurements (Lites 1996), has also used the FeI lines at 630.2 nm.

The most important improvement over the currently produced data sets from the KPVT are the precise vector polarimetry, which allows the derivation of the true magnetic field vector as compared to the current longitudinal flux measurements.

5.4.2. *Specifications*

Table 6 shows the specifications for the VSM according to which the instrument has been designed and is now under construction.

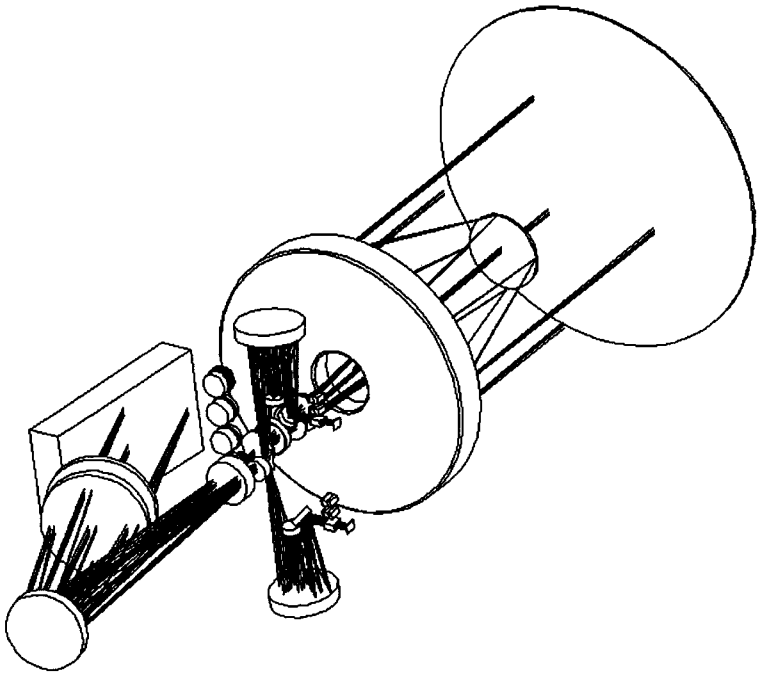

FIGURE 27. The optical layout of the SOLIS Vector-Spectromagnetograph. The entrance window is on the upper right, and the folded Littrow spectrograph is on the lower left side of the drawing.

5.4.3. *Design*

The design of the VSM faced many challenges. In particular, the following requirements have made the design effort demanding:

- compact instrument no longer than 2.5 m
- athermal optical design to keep instrument stable at varying ambient temperatures
- high guiding accuracy of better than 0.″5 rms
- low instrumental polarization of less than $1 \cdot 10^{-3}$
- large wavelength range from 630 nm to 1090 nm with constant magnification
- high spectral resolution of about 200,000
- highest possible throughput
- high energy densities of up to 0.2 MW/m^2
- high data rates of over 300 MByte/s

An overview of the optical layout is shown in Fig. 27. The mechanical layout is shown in Fig. 28.

A 50-cm effective aperture telescope is sufficient to achieve the required polarization sensitivity. To match the CCD pixel size of 16 μm per pixel (=1″) an f/6.6 beam is needed. The telescope has a Ritchey-Chrétien (RC) configuration with a two-lens field corrector to provide adequate image quality over the whole field of view, minimal geometric distortion, equal image size for all wavelengths, and a roughly telecentric beam to minimize field of view effects in the polarization modulators and the spectrograph.

The 6-mm thick entrance window reduces contamination of the optics and allows us to fill the whole instrument with helium to minimize internal seeing. The window is slightly wedged and anti-reflection coated to reduce fringes. Birefringence in the fused silica window is reduced by making it thin and oversized.

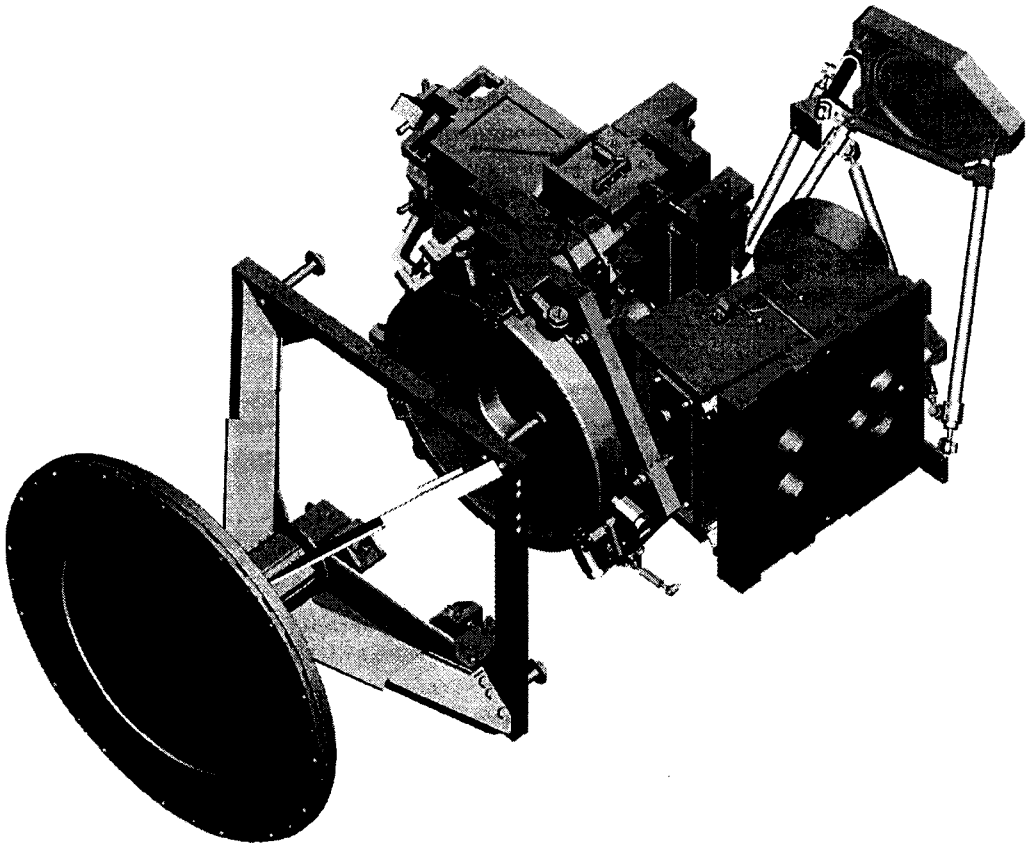

FIGURE 28. The mechanical layout of the SOLIS Vector-Spectromagnetograph. The entrance window is on the lower left, and the folded Littrow spectrograph is on the upper right side of the drawing.

The primary mirror is made of ULE to minimize temperature-induced aberrations. It will be coated with over-coated silver like all the other reflective optics to maximize the throughput. The secondary mirror is made of a silicon single crystal, which provides high thermal conductivity. Regular glass-based mirrors with their low thermal conductivity would lead to large thermal gradients within the mirror substrate and therefore to intolerable optical aberrations. A similar secondary mirror has been used in the Flare Genesis telescope (Bernasconi et al. 1999). Fans circulate the helium in such a way that the secondary mirror is cooled, which is mounted on a fast tip/tilt stage to compensate for image motion.

The requirements of low instrumental polarization and high guiding accuracy have led to an innovative design of the entrance slit area. Four linear arrays are cofocal and parallel to the entrance slit and provide an accurate guiding signal to the secondary mirror tip/tilt system and the mount. This avoids differential guiding errors and instrumental polarization and cross-talk due to a beam-splitter. The location of the limbs on the linear arrays will provide the solar disk position, the sharpness of the limb, and the sky conditions.

The fast beam will lead to an energy density of about 0.2 MW/m^2 in the focal plane. The energy that does not go to the guider arrays or through the entrance slit will be

absorbed by an actively cooled plate made out of a copper-silicon carbide composite that is used for high-energy laser optics.

The 16-μm wide, thin entrance slit covers an area of 2048″ by 1″ and is followed by the modulator packages. The entrance slit is curved to compensate for a 26-pixel spectral line curvature. The spectrograph is a Littrow arrangement with a doublet lens. The Richardson Grating Laboratory Echelle grating has 79 grooves/mm, a 63.5° blaze angle, a 204 by 408 mm ruled area, and an efficiency of about 50%, which is almost independent of the polarization state at 630.2 nm. Purely static mechanical structures will not be able to keep the grating stable enough. Therefore, the grating has actuators in two axes that are controlled by error signals generated by the CCD cameras in the final focal plane.

Since we were not able to find CCD cameras that would cover the full length of the slit with 2048 pixels, there is a beam-splitter in the spectrograph focal plane that splits the spectrum perpendicular to the spectral lines into two equal parts. The polarizing beam-splitters in front of the cameras also require a mask in the focal plane that limits the area that falls onto the detectors. Otherwise, the two polarization states would overlap. The focal mask and beam-splitter are put into the exit focal plane, which is reimaged with an Offner system that provides achromatic one-to-one reimaging with good field properties.

To achieve a high signal-to-noise ratio (SNR) in a short time, the CCD cameras must be able to read out at a high frame rate. In addition, the modulation frequency, and therefore the read-out frequency, must be faster than typical correlation times of seeing. The required SNR led to a frame rate of 300 Hz, which is also a good rate to minimize the influence of seeing. Of course, the CCDs should have the highest possible quantum efficiency and a read-out noise that is significantly below the photon shot noise. The VSM will use two 300 frame/s 1024 by 256 pixel backside-illuminated frame transfer CCD cameras from PixelVision. The cameras will take unshuttered 3.3 ms exposures of the two orthogonally polarized spectra, which are transferred to a storage area in less than 0.15 ms. Readout will occur during the next 3.3 ms exposure with 16 parallel channels at 14 bits each.

Each of the 32 channels from the two CCD cameras delivers its data via fiber optical links to an image acquisition system, which will add up frames in buffers according to the states of the polarization modulators. At least 8 frames need to be summed to reduce the initial 300 MByte/s to less than 40 MByte/s. At this reduced data rate, the accumulated data can be sent directly to the data handling system.

The polarization measurement optics consist of a polarization calibration section, a polarization modulator section, and polarizing beam-splitters.

The two polarization calibration packages (one for 630.2 nm and one for 854.2 nm) have interference filters to reduce the overall light level except for the observed band pass. Without those filters, the polarizers would be damaged due to the high flux level. The filters are followed by a dichroic polarizer and a quarter-wave plate.

For 630.2 nm, the polarizer and the quarter-wave plate can be positioned independently at various angles with respect to the entrance slit and with respect to each other. This allows us to estimate the Mueller matrices of the corrector lenses, the modulator packages, and determine small deviations of the characteristics of the calibration polarizer and the waveplate. This procedure is modeled after the successful ASP approach (Skumanich et al. 1997). For 854.2 nm, the polarizer and the quarter-wave plate are combined to provide circularly polarized light.

Each of the three modulator packages consists of one or two ferroelectric liquid crystal (FLC) modulators from Displaytech, each being a half-wave retarder at 630.2 nm, and fixed polymer retarders from Meadowlark. An FLC corresponds to a true zero-order

Stokes parameters	wavelength [nm]	construction
I, Q, U, V	630.2	interference filter $\lambda/2$ FLC at $-22.5°$ $\lambda/4$ retarder at $0°$ $\lambda/2$ FLC at $0°$ $\lambda/4$ retarder at $-22.5°$ polarizing beam-splitter at $0°$
I, V	630.2	interference filter $\lambda/4$ retarder at $0°$ $\lambda/2$ FLC at $0°$ polarizing beam-splitter at $0°$
I, V	854.2	interference filter $\lambda/6$ (at 854.2 nm) retarder at $-90°$ $\lambda/2$ (at 630.2 nm) FLC at $-20.6°$ polarizing beam-splitter at $0°$

TABLE 7. Design of the three modulator packages for the SOLIS Vector-Spectromagnetograph.

half-wave plate whose fast axis can be switched between 0° and 45° within about 40 μs. There are no polarizers in the modulator packages.

The modulation scheme for vector polarimetry is an improved version of the schemes proposed by Gandorfer (1999) and Rabin (private communication). The SOLIS VSM scheme has the advantage that both Stokes Q and U have the same noise characteristics and have slightly better SNR than Stokes V. In addition, it does not require any eighth-wave plates. Furthermore, the scheme is less sensitive to temperature fluctuations and more efficient than the scheme proposed by Gandorfer.

Table 7 outlines the constructions of the three modulator packages. The positive Q direction is defined at 22.5° with respect to the spectrograph slit and the polarizing beam-splitter.

The polarizing beam splitters are located just in front of the detectors to produce two orthogonal, linearly polarized spectral images. The images will be offset in the spectral direction with two calcite plates and a half-wave plate in between so that both ordinary and extraordinary beams travel equal optical path lengths and experience the same amount of crystal astigmatism, which is compensated for by a weak cylinder lens. The spectrograph and the associated optics are built in such a way as to minimize the instrumental polarization between the modulators and the polarizing beam splitters.

The advantage of this approach is that there are no moving parts for the polarization analysis, that the switching of the polarization states can occur rapidly, and that both polarization states are detected simultaneously after having passed through the same optics (except for the polarizing beam-splitter and the camera window).

5.4.4. *Instrumental polarization and cross-talk*

The only optical elements whose polarization properties are not calibrated regularly are the entrance window and the primary and secondary mirrors. All the other optical elements are located after the polarization calibration optics. Therefore, the combined properties of those elements can be calibrated regularly. However, we still try to minimize the polarization introduced by those elements because the coupling of instrumental polarization and non-linearities in the CCD camera read-out electronics can lead to effects that are hard to calibrate.

The static birefringence of the window is due to remaining stress from the annealing process. Measurements of the mounted window showed values of less than 3 nm. The expected crosstalk is nevertheless unacceptable. We will therefore measure the window Muller matrix with large sheet polarizers and take it into account when reducing the data.

5.4.5. *Data Reduction*

The first level of data reduction produces spectra of Stokes parameters that need to be reduced to physical quantities such as field strength, azimuth, and inclination. A quick look analysis, which provides rapid derivation of approximate values for the physical quantities will be available within 10 minutes after the observations have been taken. The fully analyzed data, which provides accurate determinations of the physical quantities, will be available within 24 hours of the observations.

Jack Harvey, Peter Povel, and Jan Stenflo taught me most of what I know about polarimetry. I thank Javier Trujillo Bueno, Fernando Moreno Insertis, Lourdes González, and Nieves Villoslada for an excellently organized winter school and the audience for many inspiring discussion. I also thank my wife Karen and my son Philip for their support during the preparation of the lectures and the manuscript. The National Solar Observatory is one of the National Optical Astronomy Observatories, which are operated by the Association of Universities for Research in Astronomy, Inc. (AURA) under cooperative agreement with the National Science Foundation.

REFERENCES

ALBERT, A. 1972 *Regression and the Moore-Penrose Pseudoinverse.* Academic.

AZZAM, R. M. A. & BASHARA, N. M. 1987 *Ellipsometry and Polarized Light.* North-Holland.

BERNASCONI, P., RUST, D., MURPHY, G., & EATON H. 1999 High Resolution Polarimetry With a Balloon-Borne Telescope: The Flare Genesis Experiment. In *High Resolution Solar Physics: Theory, Observations, and Techniques* (ed. T. R. Rimmele, K. S. Balasubramaniam, & R. R. Radick). ASP Conf. Ser., vol. 183, pp. 279–287. ASP.

BIANDA, M., SOLANKI, S. K., & STENFLO, J. O. 1998 Hanle depolarisation in the solar chromosphere. *Astron. Astrophys.* **331**, 760–770.

BILLINGS, B. H. 1990 *Selected Papers on Polarization.* SPIE Optical Engineering Press.

CHIPMAN, R. A. 1995 Mechanics of polarization ray tracing. *Opt. Eng.* **34**, 1636–1645.

CLARKE, D. & GRAINGER, J. F. 1971 *Polarized Light and Optical Measurements.* Pergamon Press.

COLLETT, E. 1993 *Polarized light: fundamentals and applications.* Marcel Decker.

DEL TORO INIESTA, J. C. & COLLADOS, M. 2000 Optimum modulation and demodulation matrices for solar polarimetry. *Applied Optics* **39**, 1637–1642.

DONATI, J.-F., SEMEL, M., REES, D. E., TAYLOR, K., & ROBINSON, R. D. 1990 Detection of a magnetic region on HR 1099. *Astron. Astrophys.* **232**, L1–L4.

DONATI, J.-F., CATALA, C., WADE, G. A., GALLOU, G., DELAIGUE, G., RABOU, P. 1999 A dedicated polarimeter for the MuSiCoS échelle spectrograph. *Astron. Astrophys. Suppl. Ser.* **134**, 149–159.

GALE, M. T., PEDERSEN, J., SCHUETZ, H., POVEL, H., GANDORFER, A., STEINER, P., & BERNASCONI, P. 1997 Active alignment of replicated microlens arrays on a charge-coupled device imager. *Opt. Eng.* **36**, 1510–1517.

GANDORFER, A. 1999 Ferroelectric retarders as an alternative to piezoelastic modulators for use in solar Stokes vector polarimetry. *Opt. Eng.* **38**, 1402–1408.

GANDORFER, A. 2000 *The second solar spectrum.* vdf.

GEHRELS, T. 1974 *Planets, Stars and Nebulae studied with photopolarimetry.* The University of Arizona Press.

HARVEY, J. E. & VERNOLD, C. L. 1997 Transfer function characterization of scattering surfaces revisited. *SPIE Proc.* **3141**, 113–127.

ISMAIL, M. A. 1986 Transmission of light by slit designed for astronomical spectrograph. *Astropys. and Space Science* **22**, 1–32.

KELLER, C. U. & SHEELEY, N. R. 1999 Scattering polarization in the chromosphere. In *Proc. of the 2nd Solar Polarization Workshop* (ed. K. N. Nagendra & J. O. Stenflo). pp. 17–30. Kluwer.

KELLER, C. U., AEBERSOLD, F., EGGER, U., POVEL, H. P., STEINER, P., & STENFLO, J. O. 1992 Zurich Imaging Stokes Polarimeter – Design Review. *LEST Technical Report* **53**. University of Oslo.

KELLER, C. U., DEUBNER, F. L., EGGER, U., FLECK, B., & POVEL, H. P. 1994 On the strength of solar intra-network fields. *Astron. Astrophys.* **286**, 626–634.

KLIGER, D. S., LEWIS J. W. & RANDALL, C. E. 1990 *Polarized Light in Optics and Spectroscopy.* Academic Press.

LEROY, J.-L. 2000 *Polarization of Light and Astronomical Observations.* Gordon and Breach.

LITES, B. W. 1996 Performance Characteristics of the Advanced Stokes Polarimeter. *Solar Phys.* **163**, 223–230.

LIVINGSTON, W. C. 1993 *Selected Papers on Instrumentation in Astronomy.* SPIE.

MACLEOD, H. A. 1969 *Thin-Film Optical Filters.* Elsevier.

MARTÍNEZ PILLET, V., COLLADOS, M., BELLOT RUBIO, L. R., RODRÍGUEZ HIDALGO, I., RUIZ COBO, B., SOLTAU D. 1999 TIP: The Tenerife Infrared Polarimeter AG Abstract Services **15**.

OAKBERG, T. C. 1995 Modulated interference effects: use of photoelastic modulators with lasers. *Opt. Eng.* **34**, 1545–1550.

PANCHARATNAM, S. 1955 Achromatic combinations of birefringent plates. Part II. An achromatic quarter-wave plate. Proc. Indian Acad. Sci. **A41**, 137–144.

POVEL, H. P. 1995 Imaging Stokes polarimetry with piezoelastic modulators and charge-coupled-device image sensors. *Opt. Eng.* **34**, 1870–1878.

POVEL, H. P., AEBERSOLD, H., & STENFLO, J. O. 1990 Charge Coupled Device Image Sensor as a Demodulator in a 2D Polarimeter with piezo-elastic Modulators. *Applied Optics* **29**, 1186–1190.

POVEL, H. P., KELLER, C. U., & YADIGAROGLU, I.-A. 1994 Two-dimensional Polarimeter with a Charge-Coupled-Device Image Sensor and a Piezo-elastic Modulator. *Applied Optics* **33**, 4254–4260.

RAMACHANDRAN, G. N. & RAMASESHAN, S. 1962 Crystal Optics. In *Encyclopedia of Physics* (ed. S. Flügge) vol. XXXV/1.

SÁNCHEZ ALMEIDA, J. 1994 Instrumental polarization in the focal plane of telescopes. 2: Effects induced by seeing. *Astron. Astrophys.* **292**, 713–721.

SÁNCHEZ ALMEIDA, J. & MARTÍNEZ PILLET, V. 1992 Instrumental polarization in the focal plane of telescopes. *Astron. Astrophys.* **260**, 543–555.

SANKARASUBRAMANIAN, K., SAMSON, J. P. A., & VENKATAKRISHNAN, P. 1999 Measurement of instrumental polarisation of the Kodaikanal tunnel tower telescope. In *: Proc. of the 2nd Solar Polarization Workshop* (ed. K. N. Nagendra & J. O. Stenflo). pp. 313–320. Kluwer.

SEMEL, M., DONATI, J.-F., & REES, D. E. 1993 Zeeman-Doppler imaging of active stars. 3: Instrumental and technical considerations. *Astron. Astrophys.* **278**, 231–237.

SEN, A. K. & KAKATI, M. 1997 Instrumental polarization caused by telescope optics during wide field imaging. *Astron. Atsrophys. Suppl. Ser.* **126**, 113–119.

SHURCLIFF, W. A. 1962 *Polarized light-production and use.* Harvard University Press

SKUMANICH, A., LITES, B. W., MARTÍNEZ PILLET, V., & SEAGRAVES, P. 1997 The Calibration of the Advanced Stokes Polarimeter. *Astrophys. J. Suppl.* **110**, 357–380.

SLATER, J. C. 1942 *Microwave Transmission.* McGraw-Hill.

STENFLO, J. O. 1984 Solar magnetic and velocity-field measurements: new instrumental concepts. *Applied Optics* **23**, 1267–1278.

STENFLO, J. O. 1991 Optimization of the LEST polarization modulation system. *LEST Technical Report* **44**. University of Oslo.

STENFLO J. O. 1994 *Solar Magnetic Fields: Polarized Radiation Diagnostics.* Kluwer.

STENFLO, J. O., KELLER, C. U., & POVEL, H. P. 1992 Demodulation of all Four Stokes Parameters With a Single CCD. ZIMPOL II - Conceptual Design. *LEST Technical Report* **54**. University of Oslo.

STOCKMAN, H. S. 1982 Differential imaging using charge-coupled image device (CCD) imagers with on-chip charge storage. *SPIE Proc.* **331**, 76–80.

SWINDELL, W. 1975 *Polarized Light.* Dowden, Hutchinson & Ross.

TINBERGEN, J. 1996 *Astronomical polarimetry.* Cambridge University Press

WAHLSTROHM, E. E. 1960 *Optical Crystallography.* Wiley.